NOVA SCHOOL OF SCIENCE & TECHNOLOGY

DEPARTMENT OF PHYSICS

MÓNICA TOMÉ DYREBY

BSc in Physics Engineering

QUANTUM EFFICIENCY OF ORGANIC SOLAR CELLS AS A FUNCTION OF TEMPERATURE AND FIELD

A STUDY OF PM6:Y6

MASTER IN PHYSICS ENGINEERING

NOVA University Lisbon
November, 2023

NOVA SCHOOL OF SCIENCE & TECHNOLOGY

DEPARTMENT OF PHYSICS

QUANTUM EFFICIENCY OF ORGANIC SOLAR CELLS AS A FUNCTION OF TEMPERATURE AND FIELD

A STUDY OF PM6:Y6

MÓNICA TOMÉ DYREBY

BSc in Physics Engineering

Adviser: Martijn Kemerink
Full Professor, Ruprecht-Karls-Universität Heidelberg

Co-advisers: Clemens Göhler
Postdoctoral researcher, Ruprecht-Karls-Universität Heidelberg

Maria de Fátima Guerreiro da Silva Campos Raposo
Associate Professor , NOVA University of Lisbon

Examination Committee

Chair: Paulo António Martins Ferreira Ribeiro
Associate Professor, NOVA University of Lisbon

Rapporteur: Susana Isabel dos Santos Silva Sério Venceslau
Associate Professor, NOVA University of Lisbon

Member: Maria de Fátima Guerreiro da Silva Campos Raposo
Associate Professor, NOVA University of Lisbon

MASTER IN PHYSICS ENGINEERING

NOVA University Lisbon
November, 2023

Quantum efficiency of organic solar cells as a function of temperature and field
A study of PM6:Y6

This document was created with the (pdf/Xe/Lua)LaTeX processor and the NOVAthesis template (v7.0.3) [1].

To Heidelberg.

Acknowledgements

Acknowledgments

I would like thank several individuals and institutions: Martijn Kemerink, Clemens Göhler, and Maria Raposo for their guidance. I am grateful to FCT NOVA University, Ruprecht-Karls-University Heidelberg, and the Kemerink Group at IMSEAM for providing the resources that made this thesis possible. Finally, I would like to thank my mother Maria Tomé, Manuel Cantanhede, Katarina Dyreby, Tiago Teles, Francisco Santos, Catarina Mendes, and Tala Al-Sunna for their support throughout this journey.

Abstract

One of the limiting factors in the power conversion efficiency of organic solar cells is the open circuit voltage. In the highly efficient non fullerene acceptor PM6:Y6 organic solar cells, open circuit voltage is still below that of inorganic solar cells. This thesis investigates the quantum efficiency of PM6:Y6 organic solar cells under various applied biases, including open circuit voltage, and at different temperatures, aiming to unravel the underlying mechanisms governing their behaviour. Notably, this study observes significant photo-current under forward bias conditions, extending beyond the open circuit voltage. Subsequent comparison of experimental data with kinetic Monte Carlo and Drift Diffusion simulations unveil the recombination kinetics surrounding the open circuit regime, demonstrating a clear dependence of geminate recombination on both bias voltage and temperature. With the maximum geminate recombination peak occurring at the open circuit voltage, suggesting a dependency in free charge generation, on these parameters.

Keywords: Organic Solar Cell, Quantum Efficiency, PM6:Y6, Open Circuit Voltage, kinetic Monte Carlo, Drift Diffusion,

Resumo

Um dos fatores limitantes na eficiência de conversão energética das células solares orgânicas é a tensão de circuito aberto. Nas células solares orgânicas PM6:Y6 de alta eficiência com o aceitador não-fullereno, a tensão de circuito aberto ainda está abaixo da tensão das células solares inorgânicas. Esta dissertação tem como objetivo investigar a eficiência quântica das células solares orgânicas PM6:Y6 sob diversas tensões, incluindo a de circuito aberto, e a diferentes temperaturas, com o objetivo de entender os mecanismos que governam o comportamento destas células. Neste estudo, observa-se uma foto-corrente significativa sob condições de polarização direta, estendendo-se além da tensão de circuito aberto. A subsequente comparação dos dados experimentais com simulações de Monte Carlo cinético e Drift Diffusion revelam as cinéticas de recombinação em torno do regime de circuito aberto, demonstrando uma clara dependência da recombinação geminada tanto no campo elétrico como na temperatura. O máximo da recombinação geminada ocorre na tensão de circuito aberto, sugerindo uma dependência na geração de cargas livres nestes parâmetros.

Palavras-chave: Células Solares Orgânicas, Eficiência Quântica, PM6:Y6, Tensão do circuito aberto, Método de Monte Carlo cinético, Drift Diffusion

Contents

List of Figures

List of Tables

Acronyms

BHJ Bulk Hetero Junction *(p. 4)*

CPD Calibrated Photo-Diode *(pp. 6, 7, 13)*
CS Charge Separated *(p. 5)*
CT Charge Transfer *(pp. 3–8, 15, 21, 26, 28, 30)*

D:A Donor:Acceptor *(pp. 2, 3)*
DD Drift Diffusion *(pp. 1, 10, 11)*

EQE External Quantum Efficiency *(pp. 1, 2, 5–14, 22, 24, 29–35)*
ETL Electron Transport Layer *(p. 4)*

FA Fullerene Acceptor *(pp. 8, 10, 23, 33)*
FF Fill Factor *(pp. 7, 21, 34)*

HOMO Highest Occupied Molecular Orbital *(pp. 2, 3)*
HTL Hole Transport Layer *(p. 4)*

IQE Internal Quantum Efficiency *(pp. 1, 2, 9, 10, 14, 15, 19–24, 29, 32–35)*

JV Current (density) Voltage *(pp. 7, 8, 10, 13, 19, 21, 23, 30)*

kMC kinetic Monte Carlo *(pp. 1, 10, 11)*

LUMO Lowest Unoccupied Molecular Orbital *(pp. 2, 3)*

NFA Non Fullerene Acceptor *(pp. 5, 8)*

OC Open Circuit *(pp. 24, 25, 29–31, 35)*

OpC Optical Chopper *(p. 11)*
OSC Organic Solar Cell *(pp. 1–12, 14–17, 19, 21–25, 29, 32–35)*

PCE Power Conversion Efficiency *(pp. 5, 7, 8, 34)*

SC Short Circuit *(pp. 6, 12, 13, 19, 21, 22, 29, 30)*
SR Spectral Responsivity *(p. 7)*

TMM Transfer Matrix Method *(p. 9)*

1 Introduction

Several world powers have recognised the need to transition towards environmentally friendly and renewable energy sources, such as solar energy[2]. One of the base components for the conversion of solar power to electrical energy are photovoltaic solar cells. This thesis specifically focuses on Organic Solar Cell (OSC) due to the increasing interest in their technology, driven by an increase in conversion efficiency to $\approx$ 20% [3], making them comparable to their inorganic counterparts. Nevertheless, various aspects of OSC operation are not clear.

The External Quantum Efficiency (EQE) and Internal Quantum Efficiency (IQE) curves of OSCs hold a lot of information about the efficiencies that govern their behaviour, such as charge dissociation, exciton diffusion, charge transport and collection. Their relation to temperature and electric field will be the focus of this thesis. The scope of which includes the analysis of the non-light biased and light biased EQE and IQE of PM6:Y6 OSCs. This particular blend was chosen for this analysis since it is a representative testbed system for modern non-fullerene OSCs. Furthermore, the thesis will involve the interpretation of experimental results through the use of kinetic Monte Carlo (kMC) and Drift Diffusion (DD) simulations, as well as a comparative analysis between these two simulation models.

It follows a structured approach, starting with Chapter 2, which establishes the theoretical foundation, introducing the EQE and IQE. Chapter 3 covers practical aspects, including EQE measurement procedures and simulation models. In Chapter 4, the focus is on analysing the average IQE ($\overline{\text{IQE}}$) under bias voltage and temperature, exploring charge recombination kinetics through the kMC model. Finally, in Chapter 5 key findings are summarised.

2

Theory and Literature Review

This chapter's objective is to establish a solid theoretical foundation by exploring the underlying mechanisms that dictate the behaviour of OSCs, such as charge transfer states, recombination, and excitons. Within this chapter, the concepts of EQE and IQE are introduced, including explanations of their calculation methods, interrelation, and sensitivity to temperature and bias conditions. Throughout the chapter, information about the PM6:Y6 blend is provided, including typical metric parameter values. This chapter sets the stage for the subsequent experimental work by providing the necessary theoretical context.

2.1 Organic Semiconductors

When considering a simple organic molecule, its Highest Occupied Molecular Orbital (HOMO) and Lowest Unoccupied Molecular Orbital (LUMO) can be thought of similarly to the valence and conduction bands in an inorganic semiconductor. From a simple organic molecule to an amorphous solid, the energy landscape is broadened due to structural disorder and the previous band-like HOMO and LUMO follow a Gaussian or exponential Density of States (DOS). As such, in organic semiconductors, which are materials composed of carbon-based molecules, charges are localised to certain molecular sites (e.g. a monomer). This localisation of charges means that charge transport is done via **hopping** from one localised state to another.

When illuminated, an electron in the HOMO can be excited to the LUMO by a photon. This process creates a hole (absence of an electron) in the HOMO, where the electron used to be. Creating a localised electron-hole pair, which is bound by the Coulomb attraction. In organic semiconductor materials, the dielectric constant is low $\epsilon_r \approx 3.5$ [5], which results in poor Coulomb screening. Thus, these charge carriers are tightly bound and are dubbed Frenkel excitons. In contrast, in inorganic semiconductors the dielectric constant can be as large as $\epsilon = 11$ [5].

To separate these two charge carriers and generate electrical current, it is necessary to introduce a Donor:Acceptor (D:A) junction. Where a donor material donates (excited)

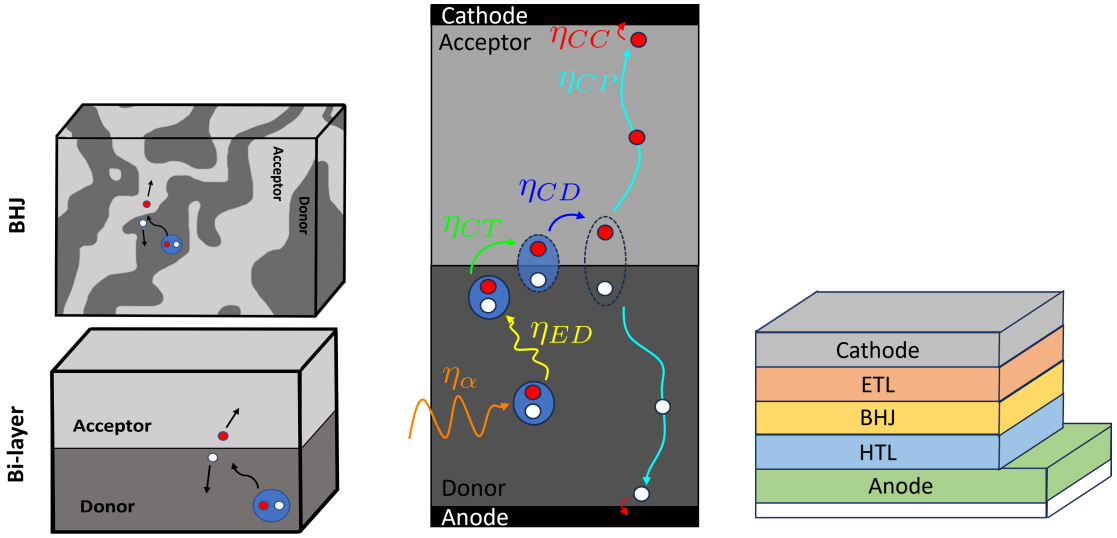

(a) (b) (c)

Figure 2.1: ; **(a)** Schematic of Bulk Hetero Junction (BHJ) OSC morphology and Bi-layer OSC morphology. The light grey material is the acceptor and the dark grey is the donor. In red the electron, in white the hole and in blue an exciton; In both architectures, the exciton diffuses to the Donor:Acceptor interface and separates. The subsequent generated charges move through their respective material (hole in donor and electron in acceptor) into their respective electrode; **(b)** Schematic of efficiencies of operating processes: absorption (η_{α}), exciton diffusion η_{ED}, CT formation (η_{CT}), charge dissociation (η_{CD}), charge transport (η_{CP}) and charge collection (η_{CC}). Based on Reference [4]; **(c)** Standard OSC architecture (non-inverted). In blue the Hole Transport Layer (HTL), in yellow the BHJ, in orange the Electron Transport Layer (ETL) and in green and grey the electrodes. At the bottom, in white, the glass substrate upon which the OSC sits.

electrons from its LUMO to the acceptor's LUMO. This electron transfer process creates a CT state, which is less tightly bound due to increased charge delocalisation. Similarly, photons can also excite the acceptor electrons and thus a hole transfer occurs from the acceptor's HOMO to the donor's HOMO.

2.2 Basic Organic Solar cell operation

While the architecture of the first OSC design included only one organic semiconductor between two electrodes, missing the crucial CT process and achieving a conversion efficiency below 1% [6]. The second design, introduced by Tang in 1986 [7], addressed the limitations of the initial OSC design, by adding a second organic semiconductor layer, creating a bi-layer OSC (see Figure 2.1(a)).

This design operates based on the following processes, each with their respective efficiencies: the photo-generated exciton diffuses to the D:A interface (η_{ED}), where the charge transfer process takes place (η_{CT}). The CT state can then dissociate generating

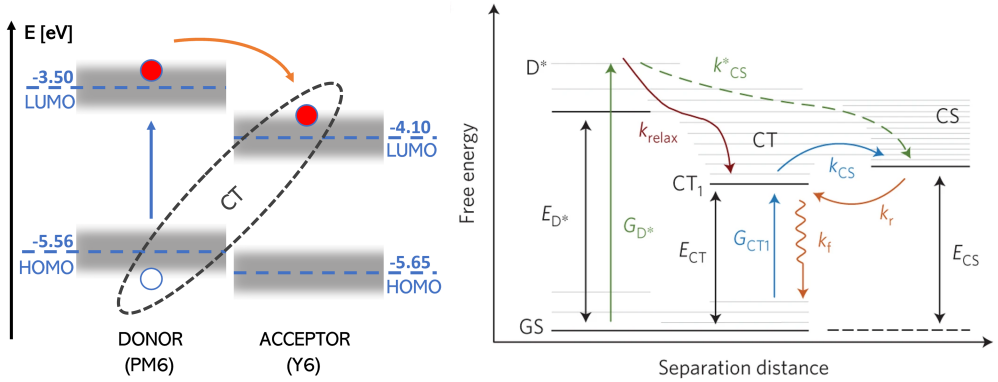

(a) (b)

Figure 2.2: **(a)** Jablonski diagram, not to scale, showcasing indirect (orange arrow) CT state formation in a PM6:Y6 OSC (energies taken from Reference [8]). In indirect CT state formation, the electron (red dot) is excited by a photon (blue arrow) from the donor HOMO to the donor LUMO and then transfers to the acceptor LUMO. The white dot represents the hole created due to electron excitation; **(b)** State diagram, taken from reference [9], highlights several processes in an OSC. Photon absorption at a rate of G^*_D generates an excited donor state D^*, which may decay into either a CT state or a charge-separated (CS) state with the rates k_{relax} and k^*_{CS} respectively. The lowest energy CT state (CT_1) can relax to the GS with k_f rate or to the CS states with a rate of k_{CS}. Inversely, the charges can recombine from CS to CT with a rate of k_r and the population of the CT_1 state from the GS can also happen via direct excitation of the CT states (transition labelled G_{CT1}).

free charges(η_{CD}), which are then transported through the donor and acceptor (η_{CP}) and collected at the electrodes (η_{CC}) [4]. See Figure 2.1(b) for schematic representation of these processes in a (bi-layer) OSC.

Keeping in mind that the donor-to-acceptor excitons have an average diffusion length of ≈10 nm [6], after which they recombine [1], to reduce current losses due to recombination, the OSC design must guarantee that photo-excitation occurs at less than 10 nm from the D:A interface. While guaranteeing that the active thickness is around the absorption length of the incident photons (≈ 100 nm for visible light [6]). As such, the Bulk Hetero Junction (BHJ) OSC design was developed (see Figure 2.1(a)). This design is comprised of a disordered blend of donor and acceptor phases, resulting in an increased D:A interface, which in turn increases the exciton dissociation probability while maintaining enough thickness for light absorption. Besides the active layer (donor and acceptor blend) of the cell, these devices feature additional layers as seen in Figure 2.1(c). The Hole Transport Layer (HTL) assists in the transport of holes to the anode. Similarly, the role of the Electron Transport Layer (ETL) is to aid in transporting electrons to the cathode.

In Figure 2.2, the processes involved in the operation of OSCs are highlighted. In Figure 2.2(a), the aforementioned exciton formation process is displayed while in Figure 2.2(b), in the blue arrow (labelled G_{CT1}), the **direct** formation of CT excitons is showcased.

[1] Annihilation of an electron-hole pair [4].

The latter process results from the direct optical electron excitation at the D:A interface (from the CT ground state). However, the resulting CT excitons do not contribute to the photo-current as much as the donor/acceptor excitation (due to their much lower absolute absorption). Additionally, in this same Figure, the direct decay from excited donor (D^*) to Charge Separated (CS) state, the transition from CT state to CS state and reciprocally are also showcased. Note that direct transitions between (D^*) and CS states fall under the hot CT state theory.

In Figure 2.2(b), the transition from CS to CT state (with rate k_r) can represent non-geminate recombination when charge carriers originate from different excitons or charge generation events, such as injection from the electrodes. Conversely, geminate recombination specifically refers to the recombination of two charge carriers originating from the same exciton. This can occur through processes like the direct decay from D^* to D state or the direct decay of CT states, as depicted in orange in Figure 2.2(b) by the transition rate k_f. These recombination processes impact the efficiency of the solar cell since they reduce the number of available charge carriers for photo-current.

Among the various solar cell donor and acceptor materials, the focus of this thesis is PM6:Y6. PM6 (Poly[(2,6-(4,8-bis(5-(2-ethylhexyl-3-fluoro)thiophen-2-yl)-benzo[1,2-b:4,5-b′]dithiophene)) -alt- (5,5-(1′,3′-di-2-thienyl-5′,7′-bis (2-ethylhexyl) benzo [1′,2′-c:4′,5′-c′] dithiophene - 4,8-dione)]) is a p-type donor polymer with an optical band gap of 1.81 eV and Y6 (2,2′-((2Z,2′Z)-((12,13-bis(2-ethylhexyl)-3,9 - diundecyl-12,13-dihydro-[1,2,5]thiadiazolo [3,4-e]thieno[2",3′′:4′,5′]thieno[2′,3′:4,5]pyrrolo[3,2-g] thieno [2′,3′:4,5] thieno [3,2-b] indole-2,10-diyl) bis(methanylylidene))bis(5,6-difluoro-3-oxo-2,3-dihydro-1H-indene- 2,1- diylidene))dimalononitrile) is a low band gap Non Fullerene Acceptor (NFA) molecule. This OSC blend consistently achieves a Power Conversion Efficiency (PCE) greater than 15% [8]. See Figure 2.2(a) for the energy levels that make up these materials.

2.3 External Quantum Efficiency

The EQE is a crucial parameter in characterising the performance of OSCs. It quantifies the efficiency with which these devices convert incident photons into collected electrons and can be defined as the ratio of collected electrons to incident photons [10]:

$$\text{EQE} = \frac{\phi_e}{\phi_{ph}^{inc}(\lambda)}, \tag{2.1}$$

where ϕ_e represents the flux of electrons that reach the external circuit and ϕ_{ph}^{inc} the flux of incident photons with wavelength λ. This definition inherently takes into account all the efficiencies associated with photo-current. With that in mind, the EQE can be described as a product of several efficiencies, each of which account for the different loss mechanisms (i.e. "exciton loss in the domain during exciton diffusion, decay of excitons at the donor:acceptor interface, decay of reformed excitons from the CT states, decay of

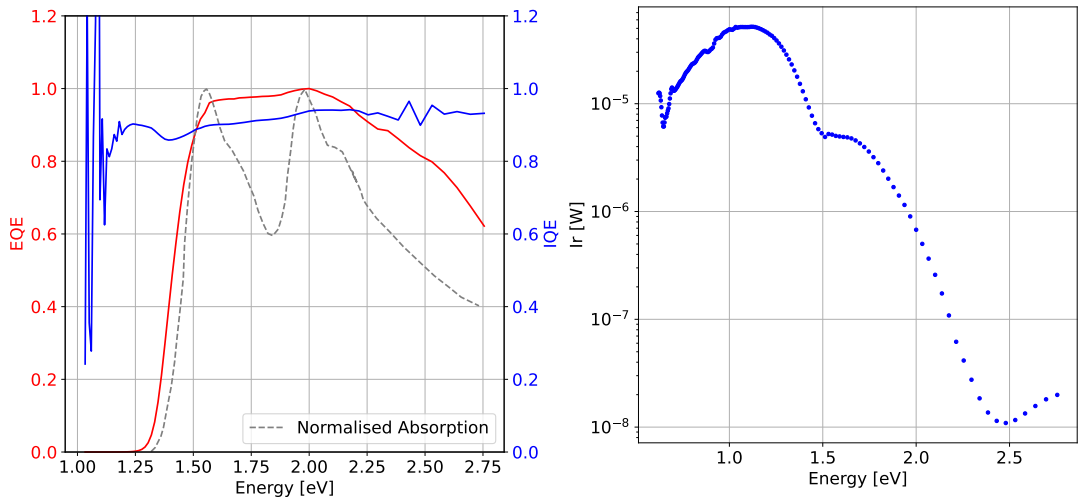

(a) (b)

Figure 2.3: **(a)**Measured IQE curve in blue, and EQE curve (normalised) in red, of a PM6:Y6 OSC at 300 K under no electrical bias. State-of-the-art PM6:Y6 OSCs typically have near unity IQE [14] and in grey is the normalised absorption spectrum of a different PM6:Y6 OSC (taken from reference [15]);**(b)** Measured Irradiance spectrum of a Spectrophotometer Lambda 1050+ halogen lamp.

the CT states" [11]) and characteristics of the OSC:

$$\mathrm{EQE}(\lambda, F, T) = \eta_a(\lambda)\eta_{ED}(\lambda, F, T)\eta_{CT}(T)\eta_{CD}(F, T)\eta_{CP}(F, T)\eta_{CC}(F, T). \tag{2.2}$$

Where η_a is the absorption efficiency and F is the electric field and T the temperature [4, 12, 13]. Notably, the EQE's sensitivity to both electrical field and cell temperature is apparent, emphasising these parameters' significance in OSC performance.

While the EQE can be calculated for each wavelength, it is often plotted against the incident photon energy[2], as is seen in Figure 2.3(a).

Given that the electron flux is the number of electrons per area and time, then $\phi_e = j_{sc}/e$, where j_{sc} is the Short Circuit (SC) current density and e the electron's charge. Analogously, the photon flux represents the number of incident photons per area and time. Considering that the irradiance of the incident light is given by power over the area, then $I_r = En_{ph}/\Delta tA$, where n_{ph} is the number of incident photons and E is the photon energy. From here it is possible to write $I_r = Ej_{ph}$.

The incoming photon flux j_{ph} is often calculated with the assistance of a reference Calibrated Photo-Diode (CPD). The relationship between EQE_{OSC} and EQE_{CPD} (provided by the diode manufacturer) is:

$$\mathrm{EQE}_{OSC} = \frac{j_{sc,OSC}}{j_{sc,CPD}}\mathrm{EQE}_{CPD} \tag{2.3}$$

[2]Photon energy is more relevant in the energetic analysis that follows the measurements.

Alternatively, the CPD manufacturer could provide the Spectral Responsivity (SR) of the CPD in A/W, which is the photo-current per incident light intensity at a λ wavelength: SR = $j_{sc}(\lambda)/I_r(\lambda)$. With $EQE_{CPD} = h\nu SR_{CPD}/e$, then the EQE_{OSC} in reference to the $I_r(\lambda)$ can be calculated by

$$\text{EQE}_{OSC} = \frac{j_{sc,OSC}}{I_r}\frac{h\nu}{e} \tag{2.4}$$

The EQE curve in Figure 2.3(a), obtained in through Equation 2.4 with the Irradiance spectrum in Figure 2.3(b), has a characteristic shape. With peaks at specific energies, that correspond to the absorption characteristics of the donor and acceptor. For example in PM6:Y6 OSCs, the absorption peak at 2.00 eV is due to excitons generated in the donor phase (PM6), and the peak at one at 1.55 eV is due to excitons generated in the acceptor (Y6). As the absorption decreases so does the EQE, for PM6:Y6 OSCs this steep drop happens at around 1.40 eV [15]. At low energies, beyond the range characterised by very high absorption in the donor and acceptor materials, the EQE typically exhibits a shoulder, which is usually attributed to the direct CT state absorption [16]. This is only visible in a logarithmic plot (see Figure A.2), and according to Toro *et al.* [15] this may not be the case for PM6:Y6 OSCs.

As per the equation 2.4, the EQE curve in Figure 2.3(a) was measured under short circuit conditions. In other words, the cell in question was measured without any applied electric field[3]. This is often the case for EQE measurements. However, there is a clear relationship between the EQE and electrical bias, as per Equation 2.2.

The relationship between solar cells and bias is often explored through the Current (density) Voltage (JV) curve which is measured under standardised testing conditions: 1000 W/m^2 of Light Power Density with AM1.5[4] at 25 ºC. This curve provides an overview of a solar cell's behaviour across a range of electrical bias conditions, as well as other performance metrics like the open circuit (OC) voltage (V_{OC}), short circuit current density (J_{SC}) and the Fill Factor (FF)[5]. These three parameters combine into the PCE (see equation 2.5) and are often displayed in the JV curve (see Figure 2.4)

$$\text{PCE} = \frac{V_{OC}\ J_{SC}\ \text{FF}}{\text{Light Power Density}} \tag{2.5}$$

In Figure 2.4, two curves are displayed. The blue curve refers to the JV curve when the cell is illuminated with AM1.5 and the orange curve refers to the JV curve of the cell when no light is shone on it, often referred to as *dark JV*.

It could be argued that standard EQE measurements are done under (almost) dark conditions [17]. For instance, the Irradiance spectrum used in EQE measurements, in Figure 2.3(b), has a **maximum** value of around 5×10^{-5} W, and the solar cell measured in

[3] In an OSC, there is a built-in field $\vec{F_{bi}}$ associated with the work function difference between the two electrodes. When the cell is biased with an applied electric field $\vec{F_{app}}$, the internal field in the cell is $\vec{F} = \vec{F_{bi}} + \vec{F_{app}}$.

[4] AM1.5 is the standard solar spectrum at the terrestrial surface under specified atmospheric conditions.

[5] The FF is the ratio of maximum power output $V_{max}I_{max}$ and $V_{OC}I_{SC}$.

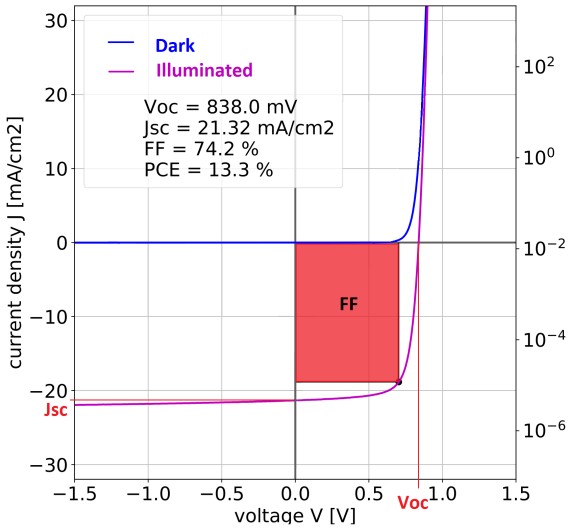

Figure 2.4: JV curve of a PM6:Y6 with a 1:1.2 donor-acceptor ratio OSC measured under AM1.5 by the Chemnitz lab. Typical values for this blend include a $V_{OC} \approx 0.8$ V, $J_{SC} \approx 24$ mA/cm^2 and a Fill Factor $FF \approx 73\%$ [8]. In the illuminated curve (in purple), from -1.50 V to V_{OC} the output current is negative, meaning the majority is being generated by the solar cell. Beyond V_{OC}, injected charges from the electrodes dictate the current going through the cell. In the absence of light (blue curve) there is no output current in the cell. Consequently, below V_{OC} the current density in the cell should be zero. In this Figure the FF is shown as a red rectangle, this is typically the case for solar cell JV curves.

Figure 2.3(a) has an illuminated area of $\approx 3.14\times10^{-6}$ m^2, then the **maximum** power density is ≈ 16 W/m^2. This value is around 60 times smaller than the 1000 W/m^2 of light power density used in standardised JV curve measurements.

For obvious reasons, solar cells are not intended to operate in the dark and in short-circuit conditions. Hence, standard EQE measurements (i.e at short-circuit and in the dark) do not reflect the efficiency of the operating processes in OSCs when used in their intended conditions. On that account, EQE measurements could be done under a light bias [18–20]. Combining this with the varying applied biases (electric field), the EQE of the cell at several points in its illuminated JV curve can be probed. Of these points, V_{OC} holds special significance since it plays an important role in the PCE and can not be studied with standard EQE measurements. However, biased EQE measurements are often done in reverse bias [13, 21–23]. In other words, when the current is negative in the JV curve (see Figure 2.4).

Considering the Coulomb interaction between the hole and electron in the CT pair, it should be expected that charge generation and, therefore, EQE spectra be bias-dependent (EQE $\propto \eta_{CD}(F,T)$). While in 2018 Ran *et al.* [21] found minimal field dependence in a PIPCP:PC61BM [6] cells, Liu *et al.* [22] found a significant field dependence in the EQE curve for a PTQ10:ZITI-C[7] cells but not as pronounced when the acceptor was switched

[6] Fullerene Acceptor (FA) OSC blend
[7] NFA OSC blend

to acceptor ZITI-N. These are just three examples of OSC blends that show different EQE behaviour. Clearly, the bias dependency of EQE curves is highly dependent on the OSC blend. Notably, for PM6:Y6, charge generation has been found to be bias independent [14] for all incident photon energies. However, since the EQE does not solely reflect charge generation (see Equation 2.2), this bias independence may not be present in the EQE curves for PM6:Y6. Moreover, the transport efficiency η_{CP} is also field dependent, meaning that a reduction in this efficiency will significantly affect the overall EQE spectrum.

From Equation 2.2, the temperature is another external parameter that can affect the EQE of an OSC. Charge carrier transport is affected by temperature, as a reduction in temperature will lead to a reduction in mobility [24]. As such, the EQE has been found to decrease with temperature for PM6:Y6 [14] and other blends [16].

2.4 Internal Quantum Efficiency

Besides the EQE, the IQE of an OSC is another way of quantifying the mechanisms that determine its behaviour. Although the IQE is defined as the ratio of collected electrons to **absorbed** photons, Equation 2.2 can be rewritten as

$$\mathrm{IQE}^t = \frac{\mathrm{EQE}}{\eta_a} \tag{2.6}$$

That is, $\mathrm{IQE}^t(\lambda, F, T) = \eta_{ED}(\lambda, F, T)\eta_{CT}(T)\eta_{CD}(F, T)\eta_{CP}(F, T)\eta_{CC}(F, T)$. As such, the IQE curve holds similar information as the EQE curve while excluding the direct influence of the absorption. Resulting in curves akin to the one in Figure 2.3(a).

The IQE of a solar cell can be determined with the measured EQE through Equation 2.7 at high reverse bias, since at high enough voltage all the charges are removed from the device, meaning that the $\eta_{ED}\eta_{CT}\eta_{CD}\eta_{CP}\eta_{CC}$ efficiencies are all unity. Thereby, the $\mathrm{EQE}(V_{bias})$ is equal to the absorption spectrum (η_a) [25].

$$\mathrm{IQE} = \frac{\mathrm{EQE}(\lambda, 0V)}{\mathrm{EQE}(\lambda, V_{bias})} \tag{2.7}$$

However, IQEs calculated using Equation 2.7 are not quantitative and need to be normalised to a calibrated IQE (IQE^t) calculated with Equation 2.6, which requires the absorbance of the active layer in the OSC [25]. To get this absorbance, one has to "obtain an accurate near-normal incidence measurement of the device reflectance", know the "optical constants of all layers" of the OSC, and employ the Transfer Matrix Method (TMM) to deconvolute the absorption for every layer [26]. To rephrase it, while the output of Equation 2.6 is a true IQE, Equation 2.7 offers an easier method to get a qualitative IQE.

Since the IQE and EQE are inherently connected, the same external parameters that affect the EQE also influence the IQE. Given that the IQE excludes the effect of absorption: the effects of temperature, applied bias and light bias on the electric processes of the OSC become more evident in IQE spectra.

Given the bias and temperature independent nature of absorption (see Equation 2.2) the IQE should follow the same trend as the EQE. As for excitation energy dependence, for PM6:Y6, the IQE has been found to be excitation energy independent [14], meaning that charge generation may not depend on the phase the excitons are generated in.

2.5 Simulations

While the EQE and IQE spectra provide insights into the OSC processes, they do so in a steady-state picture, failing to capture their dynamic behaviour over time and space. The resulting EQE curves are often fitted with analytical models that aim to reproduce the measurements and explain them. These come hand in hand with computational models like kMC and DD. This computational approach enables the exploration of the transient mechanisms that underlie OSC operations.

As an example of kMC and DD simulations applied to OSCs: In their work, Upreti *et al.* [27] were able to successfully reproduce experimental JV curves for a 75 nm thick TQ1:PC71BM[8] cell and a 115 nm thick PM6:Y6 cell, with their kMC model. Moreover, they were also able to replicate the temperature-dependence in these JVs. However, their DD model was unable to replicate the V_{OC} value for varying temperatures, with the same inputs as kMC. Consistently staying 0.17 V and 0.13 V below kMC values (and experimental) for TQ1:PC71BM and PM6:Y6, respectively. They attributed this difference to the thermal equilibrium of charges in the DD simulations.

2.6 Thesis goal

The main objective of this thesis is to study the average IQE ($\overline{\text{IQE}}$), over a set range of incident photon energies, as a function of temperature and electrical field of PM6:Y6 OSCs. With a comparison of the experimental data with the kMC and DD simulation models.

[8] FA OSC blend

3

Methodology

Chapter 3 outlines the instrumental setup and experimental procedure for EQE measurements, covering noise and sensitivity considerations. It also introduces the kMC and DD simulation models, highlighting their essential parameters for analysing OSC behaviour in diverse scenarios. Moreover, it provides specifics regarding the measured PM6:Y6 OSCs.

3.1 Instrumental set-up

The setup used to measure the EQEs of the OSCs at different temperatures and biases, as depicted in Figure 3.1, was based on the one developed by Zeiske *et al.* [18] and built by a fellow bachelor student [28]. In this setup, monochromatic light is emitted by the PerkinElmer Spectrophotometer Lambda 1050+ halogen lamp subsequently, the monochromatic light goes through an Optical Chopper (OpC) (Thorlabs MC2000B-EC) with a frequency of 263 Hz.

As such, the previously continuous light is now modulated to the frequency of the chopper. This modulated light is reflected towards the opening of a HSFS600 Linkam stage that holds the solar cell, through the two mirrors in Figure 3.1. This instrument acts as a Faraday cage, protecting the cell from external electromagnetic fields, and through it, the temperature of the cell can be controlled. It is important to mention that the temperature control setup (Linkam LNP96) relies on a Linkam Temperature Controller and Pump, as well as a Linkam liquid nitrogen dewar.

The illuminated cell will generate a current which is then amplified and converted to voltage by a FEMTO DLPCA-200 low-noise trans-impedance amplifier. As the incident light is modulated so is the cell's output current and consequently, so is the voltage. The Trans-impedance Amplifier is then connected to a Zurich Instruments MFLI lock-in amplifier (500 kHz). Note that before the MLFI there is a voltage divider guaranteeing that the input voltage is not too large for the MLFI (V div. in Figure 3.1). Through the lock-in method, the cell's modulated and amplified current can be extracted from other background signals (e.g. electrical noise). The *clean* modulated voltage is then processed

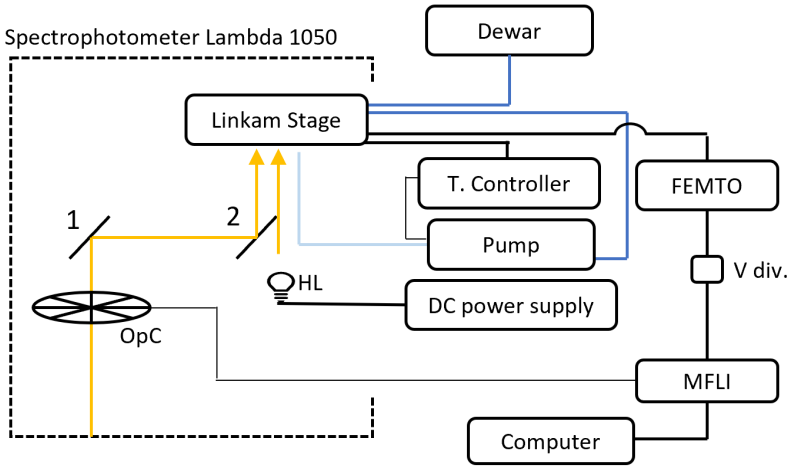

Figure 3.1: Schematic of the experimental setup used in light biased and non light biased EQE measurements. The light emitted from the spectrophotometer goes through an OpC and is then reflected with mirrors 1 and 2 onto the Linkam stage where the OSC sits. The HL lamp serves as a biasing light source and is powered by the DC power supply. To control the temperature of the OSC, the Dewar (with liquid nitrogen), Temperature Controller and Pump are used. The flow of nitrogen is designated to the lines in blue. There is an additional light blue line that details the placement of the tube redirecting evaporated nitrogen to the Linkam stage window to thwart condensation. The FEMTO transcendence amplifier and MFLI amplify the current and transform it into voltage, and employ the lock-in method, respectively. Note that the Opc sends a reference signal to the MFLI, as per the lock-in method. Finally, the computer in the setup serves as a way to control the bandwidth and incident photon energy and collect the measured data. The V divider ensures the MFLI is protected from high voltages.

and the cell's EQE versus energy (or wavelength) is plotted, as seen in Figure 2.3(a) in Section 2.2. An additional dimmable halogen lamp (HL) is also in the set-up, directly facing the Linkam stage window (0.2 cm in diameter). It is used for light biased EQE measurements and powered by a Delta Elektronika ES 030-5 DC power supply. The light from this lamp should not be modulated to the chopper frequency. As such, the photo-generated charges resulting from illumination from this second lamp should not be picked up in the EQE measurements. For typical EQE measurements, this second light source would not be present. Additionally, the evaporated nitrogen resulting from OSC cooling can be used to prevent condensation on the outside of the Linkam stage window when the gas tube is positioned in its direction. To prevent condensation or ice formation inside the stage, a nitrogen atmosphere is created within the stage by flushing the container with nitrogen gas.

As discussed previously, standard EQE measurements are done under very dim light (see Section 2.3). Hence, the output current of an OSC can be very small, even in SC conditions. Naturally, the signal-to-noise ratio is an important aspect to consider in EQE measurements, especially at low incident photon energies. Moreover, white light and electrical biasing introduce additional noise in the system. With that in mind, the FEMTO

DLPCA-200 is a low-noise amplifier, minimising its own contribution to the overall noise in the signal chain, while offering a gain of up to 10^9 V/A at low noise and acting as an adjustable electrical bias source (±10 V) used in voltage biased EQE measurements. What distinguishes this EQE measuring setup, from others, is its sensitivity. Measuring EQE curves, at SC and 300 K, down to 10^{-9} [28].

3.2 Experimental Procedure

3.2.1 Calibration

As was previously mentioned in Section 2.3, EQE measurements require the EQE or SR of a CPD. As such, three different instruments were used to obtain the Irradiance spectrum of the monochromatic light from 450 nm to 2500 nm, as depicted in Figure 2.3(b): a Silicon CPD (450-1100 nm), a Germanium CPD from (700-1800 nm) and a Calibrated Integrating Sphere (1200-2500 nm), all from THORLABS. Given that $Ir(\lambda) = j_{sc}(\lambda)/SR(\lambda)$, the j_{sc} of these three calibrated devices was measured using the EQE setup described above and the SR was provided by the manufacturer.

3.2.2 JV Curve Measurement

Before measuring the EQE of a cell, it is crucial to measure its JV curve. This preliminary step assesses the cell's performance metrics and can reveal potential degradation. It ensures that the cell aligns with the current performance standards in the literature or comes close to meeting them. Additionally, by measuring the JV curve, it guarantees a secure electrical connection between the cell and the Linkam stage contacts, thus preventing the measurement of EQEs for cells with unstable connections.

In this thesis, the JV measurements were performed using an Abet Technologies Solar Simulator inside a glove box (with nitrogen), with the cell positioned inside the Linkam stage and with a Keithley 2636B SMU (to bias and measure the current), at room temperature. Two curves were taken, one illuminated with standard illumination and one dark (see section 2.3).

3.2.3 EQE measurements

After measuring the JV curves, the Linkam stage with the solar cell is placed in the EQE setup. In this setup, the first step is to, once again, ensure that there is a stable connection between the solar cell and the Linkam stage contacts. This is done by exposing the cell to the modulated white light from the spectrometer. In the MFLI software LabOne, the voltage of the cell should also be modulated to the frequency of the chopper.

Secondly, the cell is aligned. In this process, the Linkam stage is screwed down in the Spectrophotometer and the light-path of the 530 nm green light is fine-tuned to ensure the output of the cell is maximised. This is done by adjusting the position of mirror 2 in

Figure 3.1. This step is particularly useful to guarantee the position of the cell/Linkam stage is the same in case the instrument is moved. Alternatively, it can also be indicative of a decrease in cell performance if the output is reduced.

For the actual EQE measurements, once the Linkam is connected to the temperature control instruments, all that is needed is to run a Python script. Through this script, the desired temperature can be set as well as the integration time, beginning and end wavelengths and step size. For electrical biasing, the FEMPTO needs to be manually set to the desired bias and for light biased EQE measurements, the secondary halogen lamp (HL) is switched on.

To determine the V_{OC} of the cell, with only the secondary light source, the Linkam stage was disconnected from the MFLI. The voltage output was then measured using a multimeter, with the Spectrophotometer light turned off or covered.

The EQE measurements can be used to calculate the IQE through Equation 2.7 in Section 2.4. Taking the average of this IQE over a set wavelength range, it is possible to see how this OSC metric evolves with applied bias.

3.3 Simulations

3.3.1 Kinetic Monte Carlo

In the context of OSCs, the kMC model has shown great promise [27, 29]. Briefly, in kMC algorithms a sequence of stochastic events is performed, executing a transient master Equation (see Equation 3.1) that relates the probability of two states (p_i and p_j) and their transition rates (T_{ij} and T_{ji}) at a given time (t), while maintaining a detailed balanced condition: $p_i T_{ij} = p_j T_{ji}$.

$$\frac{\partial p_j(t)}{\partial t} = \sum_{i \neq j} p_i(t) T_{ij} - \sum_{i \neq j} p_j(t) T_{ji} \tag{3.1}$$

Considering state i as the initial state, there is a set of n states $j_1, ...j_n$ to which the system can transition to. These j states are each associated with a transition rate, which determines the probability of the transition taking place. As the system transitions from one state to another, a state pathway is formed. This is one of the many possible pathways that describe the evolution of the system. As the process is repeated, distinct pathways may be taken, their average yielding the system's overall evolution [30].

Therefore, OSC-focused kMC simulations require the transition rates, associated with the efficiencies in Equation 2.2, to execute the master Equation. These rates are determined by physical models and not by the kMC simulation. As previously mentioned, these rates can be dependent on the energetic landscape in the OSC. Consequently, employing kMC simulations across a range of temperatures and fields allows for a direct comparison with experimental temperature and field dependent data (e.g $\overline{\text{IQE}}$).

In this thesis, the kMC simulations that accompany the calculated IQE versus applied bias curves were performed through a kMC model developed by Professor Martijn Kemerink and used by Upreti *et al.* [27] and Felekidis *et al.* [25].

This kMC model describes the behaviour of electrons, holes, excitons, and CT pairs, as well as their Coulomb interactions, in a three-dimensional box with set boundary conditions in the x and y directions. In the z direction, the model can employ contacts at z = 1 and at z = L, with L as the size of the active area of the OSC. The program allows for the use of an effective medium[1] instead of defining the donor and acceptor materials separately. Upreti *et al.* [27] used an effective medium in their kMC simulations, and in this thesis, it was also used. With this medium, the driving force for CT formation has to be artificially introduced, through an on-site potential barrier.

Using the Miller-Abrahams hopping rate:

$$\nu_{if} = \nu_0 \exp(-\alpha r_{if}) \begin{cases} \exp\left(-\frac{E_f - E_i \pm q\vec{r}_{if}\cdot\vec{F} + \Delta E_C}{k_B T}\right), & \Delta E > 0 \\ 1, & \Delta E \leq 0 \end{cases} \tag{3.2}$$

to describe nearest neighbour hopping from initial state i to final state f. Where E_i and E_f are the energies of the initial and final state respectively, k_B is the Boltzmann constant, $\vec{r}_{ij}$ is the vector connecting the initial and final sites, $\vec{F}$ is the applied electric field, $\pm q$ the elementary charge for electrons(+) or holes(-), ν_0 is the attempt to hop frequency, and α is the localisation length. Finally, ΔE_C describes the change in Coulomb energy, taking into account the interactions of the charge in question with all other charges in the device, including image charges. Additionally, these state energies follow a Gaussian distribution.

The recombination of excitons and CT states is governed by their, respective recombination rates: ν_{ex} and ν_{CT} respectively. Concisely, excitons recombine when an electron and a hole occupy the same site, while CT states recombine when they are in neighbouring sites. Finally, exciton diffusion is also accounted for in this model.

As detailed in the documentation for the kMC simulation model used [31], to mimic Ohmic contacts[2], buffered contacts should be utilised. In this kMC model, charges cannot be injected into already occupied states. This can lead to charges being injected and immediately extracted. Consequently, not a lot of injected charges can penetrate deeper into the effective medium. To minimise this, the semiconductor layers adjacent to the contacts act as "buffer layers". When the number of occupied states at equilibrium in this layer (calculated as the integral of the Fermi distribution times de DOS) is larger than the number of charges, injection from the contacts can happen. If not, there will be no injection.

[1] The term *effective medium* is used to describe the active area of a OSC without having to define two different materials and an active area morphology. In this *material*, the energetic landscape is defined by the HOMO level of the donor and the LUMO level of the acceptor.

[2] Ohmic contacts act as infinite reservoirs of charge carriers to be injected in or extracted from a semiconductor

To determine the recombination constant k of the system described by the parameters in Table A.1, it is necessary to run several kMC simulations with varying generation rates G. When the recombination rate R, at different generation rates, is plotted against the free carrier density n, the recombination constant can be extracted through data fitting of $R = kn^x$, with x indicating the order of recombination (e.g. when $x = 1$ recombination is monomolecular/geminate, when $x = 2$ recombination is bimolecular). See Figure A.1 in the Appendix A, for the curve fitting used to extract the recombination constant when fitting the recombination as bimolecular k_2. Note that to obtain k_2 from the kMC simulations, blocking contacts were used (i.e. no injection, no extraction and no image force potential).

To obtain the $\overline{\text{IQE}}$ as a function of applied bias, the net escape yield was extracted for each simulated applied bias. The net escape yield is calculated as $(-j_{n,an} + j_{n,cat} + j_{p,an} - j_{p,cat})/j_{abs}$, where $j_{n/p,an/cat}$ is the current density of the electrons/holes extracted at the anode/cathode and j_{abs} is the current density associated with light absorption. In other words, the net escape yield is the yield of charges extracted at the correct contact or the $\overline{\text{IQE}}$.

3.3.2 Drift Diffusion

A factor to keep in mind during any simulation is the computational cost. The Drift Diffusion (DD) simulation model is less costly than the kMC. As such, it is often used in tandem with, or in replacement of kMC [14, 27].

In the context of OSCs, this model describes the movement of the charge carriers in the active layer of the cell. Is does so by solving Poisson's Equation $\nabla^2 V = -\rho/\varepsilon_0\varepsilon_r$, and the continuity Equations (in steady state):

$$\frac{\partial j_p}{\partial x} = q(G - R) \tag{3.3}$$

$$\frac{\partial j_n}{\partial x} = -q(G - R) \tag{3.4}$$

Which describes how the carrier concentration changes with position, for holes j_p and for electrons j_n. Just as in kMC, temperature and field influence the DD simulations. While temperature defines the thermal energy of the system, bias directly impacts the drift diffusion Equations (see Equation 3.6 for holes and electrons, respectively) that feed into the continuity Equations.

$$j_p = -qn\mu\frac{\partial V}{\partial x} - qD\frac{\partial p}{\partial x} \tag{3.5}$$

$$j_n = -qn\mu\frac{\partial V}{\partial x} + qD\frac{\partial n}{\partial x} \tag{3.6}$$

Alongside the kMC model, a DD model was utilised to simulate the average IQE. This was done to directly compare the two models. The DD model, also developed by Professor Martijn Kemerink at IMSEAM, was previously used by Upreti *et al.* in reference [27].

This one-dimensional DD model, with electrons and holes, uses an effective medium with size L and two contacts, one where bias is applied (left contact where x=0) and a grounded one (right contact at x=L). In this model, charge recombination is defined by the bimolecular recombination rate: $R = k_2 n_f p_f$, where k_2 is the recombination rate constant and n_f and p_f the electron and hole density, respectively. To describe the motion of charge carriers the DD model can be set to utilise the band transport model or the extended Gaussian disorder model by Pasveer *et al.* [32].

Briefly, the model by Pasveer *et al.* [32] can determine the mobility of the charge carriers in a disordered Gaussian DOS, at different temperatures, carrier densities and electric field. As such, it can be used in the context of a DD simulation to emulate the hopping of charge carriers in a kMC simulation, at a given attempt to hop frequency, energetic disorder and nearest neighbour distance. Additionally, the DD model allows for the usage of the integral of the Fermi distribution over the DOS at the contacts, in order to mimic the buffered hopping contacts in the kMC model described above. Furthermore, in this DD model, the relation between the diffusion coefficient and the mobility was determined by the generalized Einstein Equation [33].

In order to calculate the net escape yield (or $\overline{\text{IQE}}$), this model implements an additional minor perturbation peak to the background charge generation rate G. This peak is applied to each point within the active material, and the number of points in the effective medium is determined by: $N = L/dx + 1$, where dx is the mesh size. Therefore, the $\overline{\text{IQE}}$ at each point x at an applied bias of V is determined by:

$$\overline{\text{IQE}}(V) = \frac{1}{N} \sum_{x=0}^{x=L} \frac{|j(x,V) - j_0(V)|}{qdGdx} \tag{3.7}$$

Where $j(x,V)$ is the current density of the cell at a given bias V, when the perturbation peak is applied to position x, $j_0(V)$ is the current density in the effective medium with the background generation rate and V bias, q is the elementary charge and dG is the perturbation peak strength in m^3/s. Utilising the parameters in table A.2 (taken from reference [27]) and a k_2 calculated from the kMC simulations as detailed above, a $\overline{\text{IQE}}$(V) curve can be determined [27, 34].

On a final note, just as the kMC model, this model allows for the addition of traps in the DOS. These will not be used in the DD or kMC simulations.

3.4 The solar cells

For this thesis, the cells used were produced by the team at the Deibel Lab at Chemnitz University. The Chemnitz OSCs, featuring an active area of 4 mm^2, were composed of the following layers and thickness: ITO, BM-HTL (35 nm), the active layer (100 nm), BCP (5 nm), and Ag (150 nm). The PM6:Y6, with a ratio of 1:1.2, at the time of production, was 2 months old, and the PM6:Y6 layer was not annealed after spin coating. Moreover, the PM6:Y6 solution was in chloroform (CF) + 0.5% chloronaphthalene (CN).

After production, these cells were encapsulated, in the glove box, by placing a clean glass coverslip over a drop of Ossila encapsulation epoxy in the intended area of the cell. Followed by 20 minutes under UV-light to harden the epoxy. This process is meant to protect the cell from moisture and oxygen.

4

Results and Discussion

This chapter presents an analysis of PM6:Y6 EQE and IQE curves. Including a brief analysis of the standard PM6:Y6 EQE and IQE curves, which serve as the foundation for the subsequent sections of this Chapter. It establishes the expected EQE curve values and spectral shape, while also providing an initial exploration of bias dependency within the EQE and IQE. The primary focus of this Chapter centres on understanding the average light biased IQE versus applied bias curve ($\overline{\text{IQE}}(V)$) behaviour, as it converges towards V_{OC} and beyond, offering insights into the underlying charge recombination kinetics, and temperature effects, operating in OSCs. Additionally, this Chapter showcases the replication of this curve using the kMC and DD models. Beyond the IQE versus bias voltage analysis, this Chapter also delves briefly into the following aspects: Temperature-dependent variations in EQE and IQE, shedding light on the impact of thermal energy; Noise analysis, which details the sources of noise in light-biased EQE measurements; a comparative study between light-biased and non-light-biased EQE measurements; and an analysis of the bias and excitation energy dependence of the EQE and IQE curve shape.

4.1 Standard EQE curves

Following the procedure detailed in Section 3.2, several standard (non light biased) PM6:Y6 EQE curves were measured at 300 K, with biases from -2.00 V to 0.25 V. The measured OSCs were produced by the Deibel Lab (see JV curve in Figure 2.4 in the 2) and the output EQE spectra are in Figure 4.1. Typically, SC EQE measurements of state of the art PM6:Y6 OSCs have EQEs closer to 1, unlike in Figure 4.1, where the high energy plateau is closer to 0.1. This lower EQE could be attributed to OSC degradation.

With the logarithmic scale in Figure 4.1(a), it is possible to see the presence of noise in the low energy incident photon region. This noise, as detailed by Zeiske *et al.*[18], increases with the intensity of the applied field. As such, the curve at -2.00 V has a much higher noise floor (around 2×10^{-7}) than, for instance, the curve at 0.00 V (does not reach the noise floor in the measured energy range). According to Zeiske *et al.*[18], this increase in noise is due to the shot noise induced by the bias current associated with the biasing

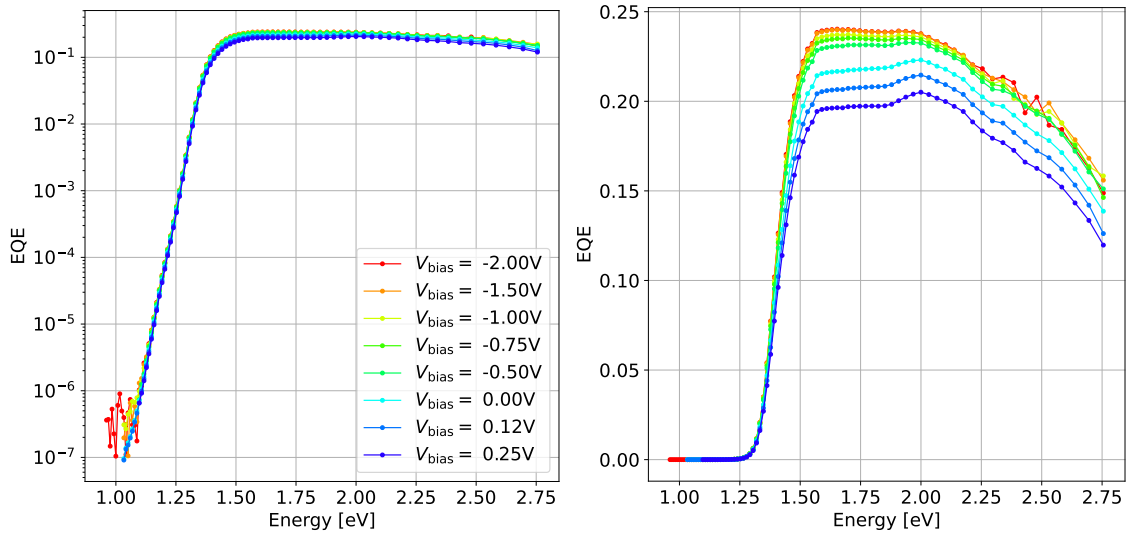

(a) (b)

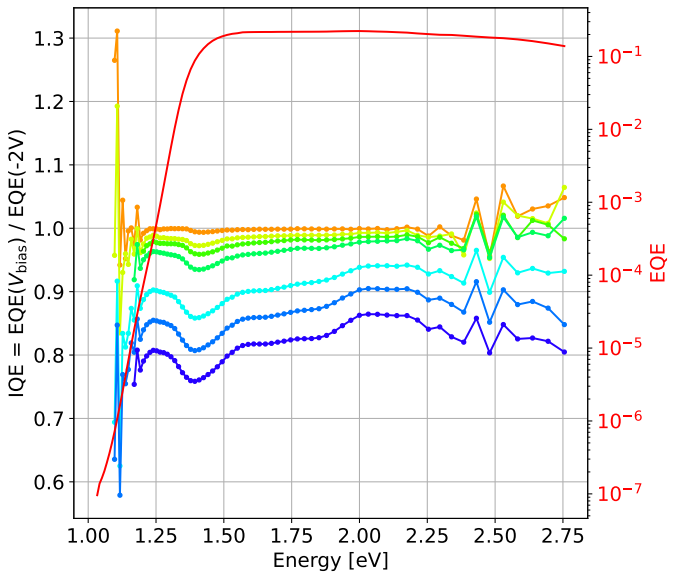

(c)

Figure 4.1: **(a)** Logarithmically scaled, non light biased EQE curves with varying electrical bias from -2.00 V to 0.25 V, obtained at 300 K; **(b)** Linear scale, non light biased full EQE curves with Varying electrical bias, obtained at 300 K; **(c)** Non light biased IQE curves with electrical biases from -1.50 V to 0.25 V at 300 K.

electric field.

The EQE curve decreases as the bias goes from -2.00 V to 0.25 V. This is more noticeable in the linear scale EQE plot in Figure 4.1(b). Interestingly, the spectral shape of the EQE is not field independent. This will be discussed further in Section 4.2.4.

As discussed in Chapter 2, the EQE curve displays a steep drop for photon energies below 1.40 eV, and a shoulder in the low energy region below 1.20 eV as seen in Figure 4.1(a). Noticeably, there is a lack of bias dependence in the low energy shoulder (see Figure A.2

in the Appendix A for the normalised close up of the EQE curves). Additionally, in the same Figure, in the very low energy section (below 1.10 eV) there is a shoulder related to trap absorption. Which, is not visible in the higher bias curves due to the increase in noise floor.

The measured EQE curves, at -1.50 V until 0.25 V, were normalised to the EQE curve at -2.00 V, as per Equation 2.7, resulting in the IQE curves in Figure 4.1(c), along with the SC EQE. In these curves, there are several discernable regions: the very high energy and very low energy region which can be disregarded as they are noisy; the first plateau from 1.95 eV to 2.30 eV; and the second plateau from 1.55 eV to 1.90 eV. The former can be attributed to excitons originating at the donor material (PM6) and the latter to acceptor (Y6) excitons. These same plateaus are present in the linear scale EQE in Figure 4.1(b). Additionally, in the low energy region, the shoulder at 1.20 eV is also present.

As previously mentioned, shoulders with energy below the known donor and acceptor absorption peaks are usually attributed to the CT states [16]. However, Toro *et al.* [15], claim this shoulder in PM6:Y6 EQEs is due to the "thermally excited Vibronic states of S_0 to the Vibronic ground state of S_1" in the Y6 material, "with little to no absorption from CT states or traps". They reach their conclusion in part due to temperature dependent EQE measurements, which will be discussed in Section 4.2.1.

Just as in the EQE curves, there is a decrease in IQE, as the applied bias increases, which is non linear, and will be discussed in detail in Section 4.2.

4.2 Light biased EQE and IQE curves

As previously mentioned, non light biased quantum efficiency curves are typically acquired under nearly dark conditions. While this setup is advantageous for reducing non-geminate recombination[14], it limits the information that can be extracted from these measurements. With light biased quantum efficiency measurements, it is possible to probe different points in the JV curve of the OSC. In particular, the open circuit point, which is inaccessible in standard EQE measurements and crucial for the PCE. Through these light biased EQE and IQE curves, one can delve into the loss mechanisms that limit the V_{OC} in PM6:Y6 blends.

With this in mind, light biased EQE curves were obtained for a PM6:Y6 OSCs, also produced by the Deibel lab. The measured JV curve, in Figure A.3 in the Appendix A, has a PCE of 5.915%, which is below what is expected for PM6:Y6 OSCs. However, the overall shape is satisfactory, displaying minimal leakage. The J_{SC} of ≈- 25.7 mA/cm^2 is typical for PM6:Y6, but the V_{OC} at 0.6 V is below typical values. The FF is particularly low, reaching only 38.3%.

Table 4.1 displays the measured V_{OC} with the OSC at 300 K, 250 K and 200 K at the same illumination intensity measured with the bias light. Notably the V_{OC} decreases slightly as the temperature increases, following a linear trend (see Figure A.4 in the Appendix A). Which, aligns with findings in the existing literature [14, 16]. Considering

that V_{OC} depends directly on the built in voltage of the cell [35]. Then, the built in voltage in this cell does not vary greatly with temperature. As such, it could be argued that the internal field, in the OSC, is the same for these three temperatures at the same applied bias.

Table 4.1: Temperature dependent V_{OC} (measured with the biasing light) light biased EQE at short circuit.

T[K]	V_{OC} [V]	$\overline{\text{EQE}}$ at SC
300	0.45±0.01	0.206 ± 0.005
250	0.49±0.01	0.194 ± 0.004
200	0.54±0.01	0.159 ± 0.003

Starting with the EQE measurement at 200 K, followed by the ones at 250 K and 300 K, all measured at the same pixel in this cell, with light bias. These EQE plots were acquired under varying electrical bias, from -2.00 V to 1.50 V, and were specifically measured at both V_{OC} and 0.00 V SC. In Figure 4.2(a), the EQE plot at 300 K is displayed. These light-biased EQEs have a similar shape to the non-light-biased ones (see Figure 4.1(a)), excluding the new low-energy bump (below 1.18 eV) and new high-energy bump (ranging from 2.33 eV to 2.75 eV), which will be discussed in Section 4.2.2. Moreover, in Table 4.1, is the average light biased EQE (between 1.44 eV and 2.20 eV) measured at SC, for each temperature. As previously mentioned, at 300 K the average EQE, of a PM6:Y6 OSC, should be close to 1. Clearly, this is not the case and can be attributed to the below state-of-the-art OSC and the added recombination introduced by the extra photo-generated charges, from the light biasing, which recombine non-geminately with the measured charges.

In terms of the EQE behaviour, it decreases as the electrical bias increases in the reverse bias regime. However, beyond V_{OC}, the EQE starts to increase. This pattern is consistent in the plots for the other two temperatures, as shown in Figure A.6 in the Appendix A. For the 300 K EQE curves, the increase beyond V_{OC} is not present. This is most likely due to degradation of the OSC: during the course of the last 300 K measurements (from 0.75 V to 1.50 V) the V_{OC} went down to 0.41 V.

The EQE curves, for each temperature and electrical bias, were normalised to the EQE curve at -2.00 V, as per Equation 2.7. The resulting IQE curves, at 300 K, are in Figure 4.2(b), along with the SC EQE. For the other two temperatures see Figure A.7 in the Appendix A. The same regions in the non light biased IQE curves are also present in these, except for the low energy shoulder which is less noticeable, due to an increase in the noise floor (see section 4.2.2). As per the nature of this IQE calculation, the bias dependency mirrors the observed trend in the previous EQE plots. This is not as clear for the measurements at 300 K, as discussed prior.

Taking the IQE average between 1.44 eV and 2.20 eV, for all three temperatures and plotting it against the applied bias, results in the three curves in Figure 4.3(a). Where,

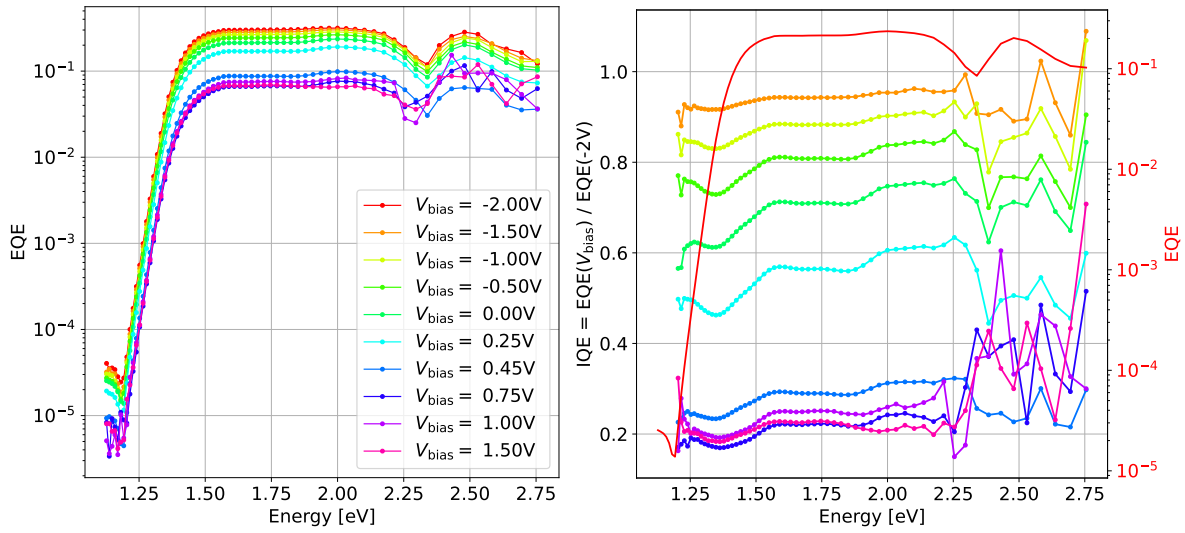

(a) (b)

Figure 4.2: **(a)** Experimentally obtained light biased EQE versus energy plots, of the same PM6:Y6 solar cell at 300 K exposed to light bias and varying electrical bias from -2.00 V to 1.50 V; **(b)** Obtained light biased IQE curves for biases from -1.50 V to 1.50 V at 300 K. The highly noisy low energy section (below 1.25 eV) is not displayed.

from -1.50 V to V_{OC} (for each temperature), the IQE decreases non-linearly, which is in accordance with the kMC simulations by Upreti *et al.*[27] and the pBTTT:PCBM 1:4 OSC[1] measurements by *Zusan et al.* [23]. Furthermore, within this bias range, there is temperature dependence, where the average IQE at 300 K is consistently above the ones at 250 K and 200 K. Due to the temperature-dependent nature of charge carrier hopping [36], charges in a OSC lattice at 300 K are less likely to get trapped in the DOS and recombine, which explains the consistently larger $\overline{\text{IQE}}$. Beyond V_{OC}, as depicted in Figure 4.3(a), the $\overline{\text{IQE}}$ exhibits an increase with bias for the measurements at 200 K and 250 K. However, the curve at 300 K does not follow the same trend. As previously explained, this discrepancy is most likely a result of cell degradation in the last three 300 K measurements. For the curve at 200 K, in Figure 4.3(a), the $\overline{\text{IQE}}$ reaches larger values than in the reverse bias regime. A possible reason for this increase is an unintentional modulation of the injected charges, which constitute the majority of charge carriers in the OSC beyond V_{OC}, resulting in their detection by the lock-in method.

Briefly, in the JV curve at room temperature (Figure A.3), the current at 1.00 V is ≈ 0,0036 A and at -1.00 V the absolute current is ≈ 0.0009 A. Considering that, according to Figure 4.3(a), there is photo-current in the forward regime, then at 1.00 V the injected current is 0.0027 A, at least. In other words, at 1.00 V, injected charges constitute, at least, 75% of the current. In the EQE measurements, the light intensity is more than 60 times smaller than in JV measurements, and the current output at -2.00 V is only 10^{-6} A. As

[1] FA OSC

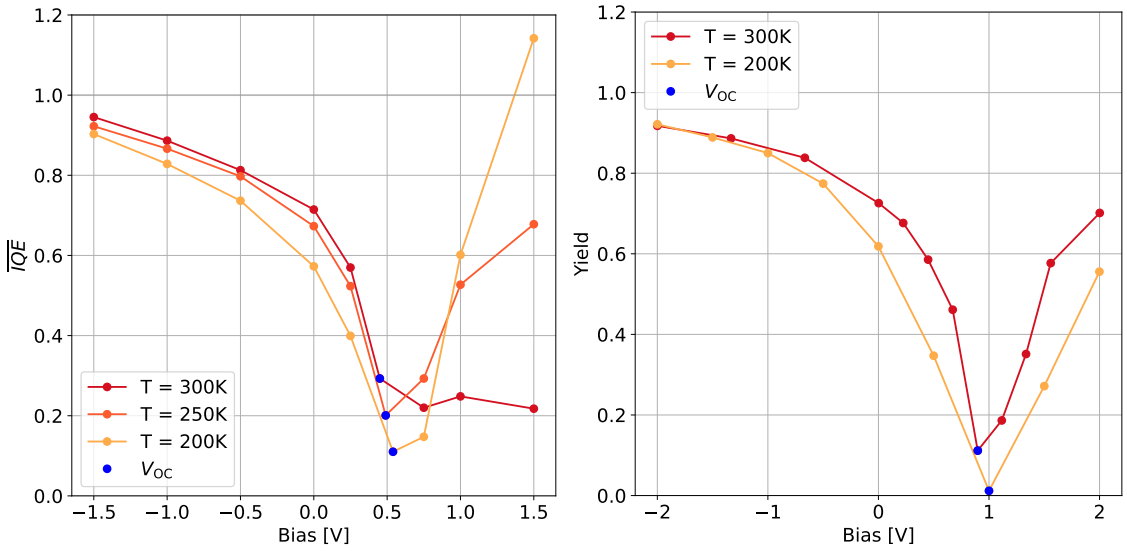

(a) (b)

Figure 4.3: **(a)** Experimentally obtained $\overline{\text{IQE}}(V)$ curves, for photon energies between 1.44 eV and 2.20 eV, for 300 K, 250 K and 200 K. V_{OC} for each temperature is highlighted in blue. The lines serve as a visual aid; **(b)** Net escape yield from the kMC simulations at 300 K and 200 K

such, injected charges at 1.00 V make up $\approx 100\%$ of the total current. Nevertheless, not all the current in the regime beyond V_{OC} can be attributed to the injected charges, as the shape of the EQE and IQE curves in this bias range are consistent with those below V_{OC}, displaying the same donor and acceptor regions.

These $\overline{\text{IQE}}$ curves where replicated, in Figure 4.3(b), through the kMC model detailed in Chapter 3 for 300 K and 200 K. Here the same bias and temperature dependency were replicated by the model. For easier comparison between kMC and experimental data, Figures 4.4(a) and 4.4(b) were plotted. In these two Figures, for both temperatures, at reverse biases, the kMC curves align fairly well with the experimental data. However, there is a clear V_{OC} offset between the simulated and measured curves. According to Upreti *et al.*[27], this kMC model is able to reproduce the V_{OC} of PM6:Y6 OSCs with similar thickness at 300 K and 200 K. Thus, this offset can be easily explained by the already reduced V_{OC} (≈ 0.6 V), OSC degradation during measurements, and the reduced light intensity as $V_{OC} \propto nk_BTq^{-1}\ln(I)$.

Additionally, there is a vertical offset between the simulated and experiential $\overline{\text{IQE}}$ at V_{OC}, which is ≈ 0.18, for both temperatures. That is, at V_{OC} the kMC underestimates the $\overline{\text{IQE}}$ by 0.18. This could be attributed to the fact that during EQE measurements at V_{OC} the OSC was not precisely at Open Circuit (OC) since the modulated light was not taken into account when measuring V_{OC} with the multimeter. That is, the V_{OC} of the cell, during the EQE measurements is a little larger than the applied V_{OC} bias voltage. As such, this minor difference in the kMC and experimental data could be due to the lack of exact OC

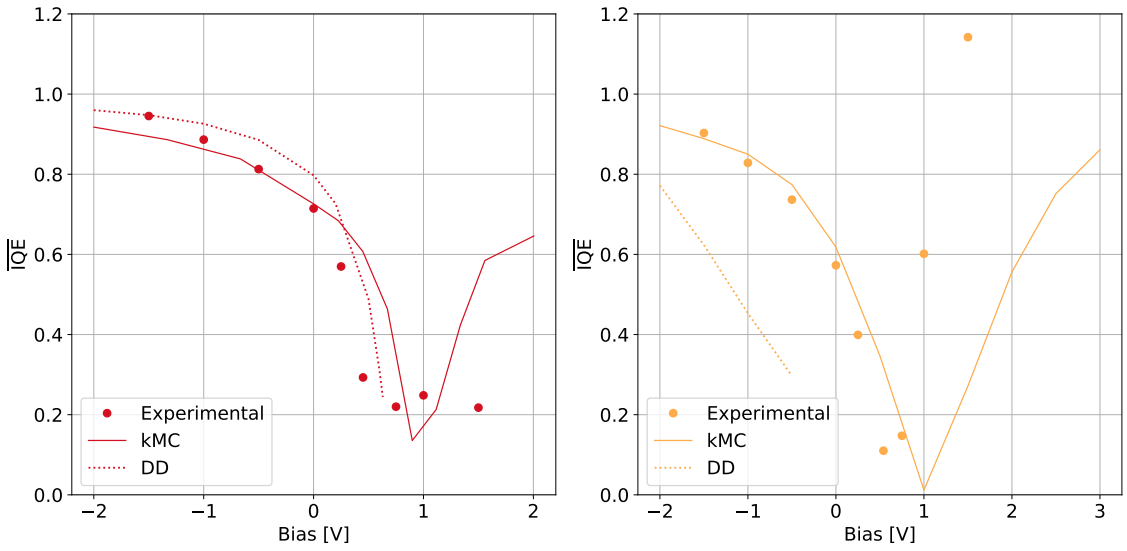

Figure 4.4: **(a)** Experimentally obtained, for photon energies between 1.44 eV and 2.20 eV, $\overline{\text{IQE}}(V)$ data (symbols), simulated kMC net escape curve (solid line), and simulated DD yield (dotted line), for 300 K; **(b)** and for 200 K.

conditions in the measured data.

For both temperatures, the experimental and simulated curves reach their minimum at V_{OC}. In the experimental curves, the $\overline{\text{IQE}}$ is non zero at V_{OC}. That is, charges are still extracted from the correct electrode in the absence of an internal field. This is also present in the simulated curve at 300 K. As discussed by Upreti *et al.*[27], the presence of photo generated charges at OC is counterbalanced by an injection current, which should guarantee that j = 0 mA/cm^2 at V_{OC}, as per the definition of OC. However, at 200 K, in the kMC simulation, the net escape is very close to zero at V_{OC}. This is in line with the reduction of injection current at lower temperatures.

In the forward bias regime, neither the 300 K nor the 200 K experimental data are reliable, either due to degradation or injected charge modulation. With that in mind, the kMC simulations were repeated, in the forward bias regime, for 250 K and plotted in Figure 4.5, along with the experimental data shifted horizontally by 0.5 V and vertically by -0.18. Although the simulated curve shows irregular fluctuations, the overall trend follows the experimental data. That is, provided the measured curves at 250 K are not affected by injection interference, the kMC simulation curve shape aligns quite well with the experimental data, both in the forward and reverse bias regimes.

Considering a built-in voltage of 0.50 V (similar to V_{OC} as per Table 4.1) then the internal field in the OSC at +1.00 V is the same as at 0.00 V. Under this assumption of lack of injected charge modulation in the 250 K experimental data, from 0.00 V to 1.00 V the $\overline{\text{IQE}}$ decreased by 22%, which translates into an increase in recombination by 22%, exclusively

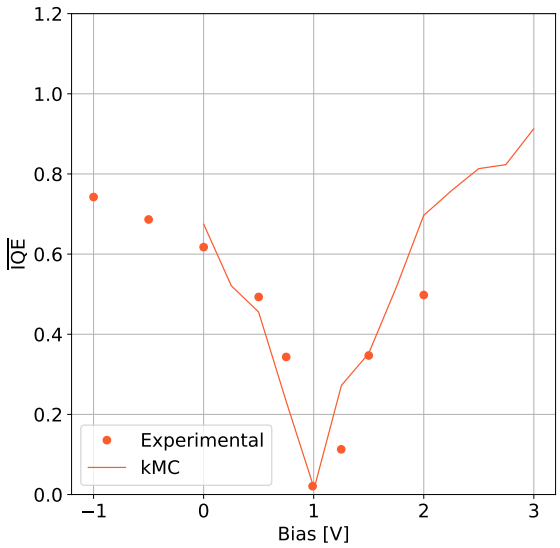

Figure 4.5: **(a)** Experimentally obtained, for photon energies between 1.44 eV and 2.20 eV, $\overline{\text{IQE}}(V)$ data (symbols) shifted horizontally by 0.5V and vertically by -0.18 at for 250 K, simulated kMC net escape curve (solid line) at for 250 K

due to injected charges recombining with the photo-generated charges. Repeating this thought process in the kMC simulations, which have a built-in voltage of 1.04 V, at 250 K: from 0.50 V to 1.50 V the net escape decreased by 23%. In other words, through the kMC simulations or the $\overline{\text{IQE}}(V)$ curve it is possible to quantify the increase in the recombination of photo-generated charges with injected charges.

Along with the net escape yield, the kMC simulations also provide the total net escape, geminate and non geminate recombination yields and CT and exciton recombination yields. These were plotted for 300K and 200K, along with the net escape yield, in the two plots in Figure 4.6. From these, it is evident that the net escape mirrors the opposite behaviour of the geminate recombination yield, regardless of temperature. At V_{OC} (where the net escape reaches its minimum) germinate recombination is maximized. Noticeably, for the curves at 300 K, the CT recombination is entirely geminate, which indicates that the electric field has a direct impact on the CT recombination. However, at this bias and beyond, most of the recombination is non geminate. This is most-likely due to the presence of injected charges in this bias range, recombining mostly with each-other and with the photo-generated charges. Beyond V_{OC}, germinate recombination decreases and the net escape increases again, staying below the net escape at high reverse bias (due to increased recombination with the injected charges). The 200 K curve, at V_{OC}, has a net escape of approximately zero. Which, is a consequence of larger germinate recombination yields (when compared to the curve at 300 K), due to decreased mobility [24] and injection. As such, in these simulations, both thermal energy and field play a significant role in CT charge recombination. Additionally, in the 200 K curve, compared to the curve at 300 K, there is considerably less non-geminate recombination in the same bias (see Figure A.8 in the Appendix A). Which, is due to the reduced injection at 200 K.

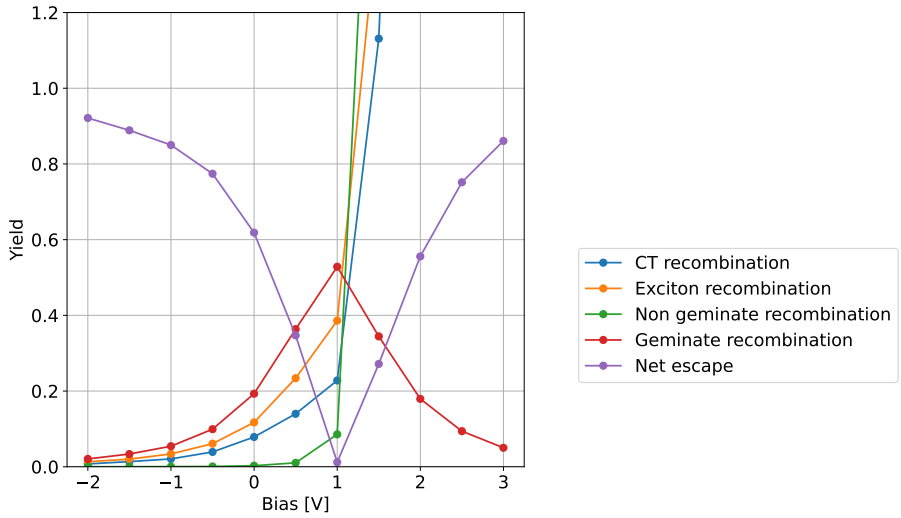

(a)

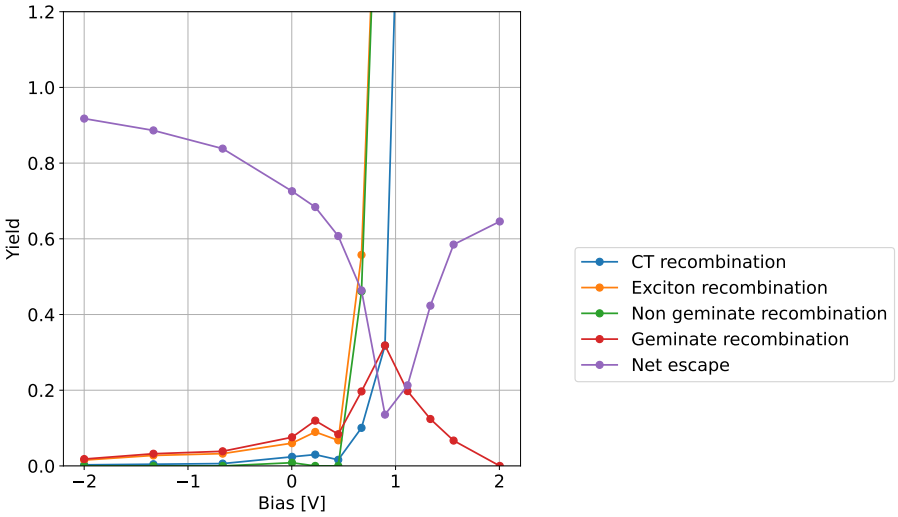

(b)

Figure 4.6: Yield output of the kMC simulations versus bias. The net escape (in purple) which refers to the charges extracted at the correct contact, geminate recombination yield (in red) and non geminate recombination yield (in green), and exciton and CT recombination which refer to the recombination of excitons and CT states irrespective of their origin (photo-generated or not). Note that Yield Gem. rec. + Yield Non Gem. rec. = Yield CT rec. + Yield Exciton rec. **(a)** At 200 K; **(b)** and at 300 K; For a complete plot see Figure A.8 in the Appendix A.

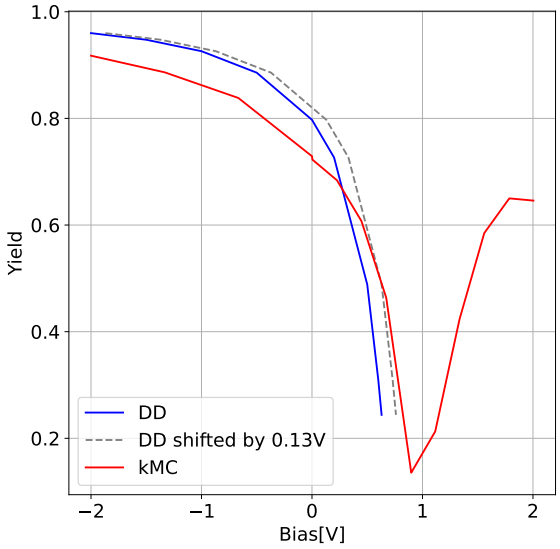

Figure 4.7: Original (in blue) and horizontally shifted (in grey) yield output versus bias of DD simulation and kMC simulation (in red). All curves at 300 K.

The implication that CT and exciton recombination is bias dependent does not necessarily contradict the findings by Toro *et al.* [14]. Their conclusions were achieved through transient measurement techniques (temperature-dependent time-delayed collection field), unlike EQE. That is, their measurements can capture non equilibrium effects in charge generation. A possible interpretation that combines Toro *et al.*'s work with the output of the kMC simulations is: that while CT dissociation might be field independent, reduced hopping (due to reduced field or temperature) keeps the generated free charge carriers in close proximity, where they can reform a CT state and recombine geminately. That is, effective charge separation is bias dependent.

As previously mentioned, in order to match the DD to the kMC simulations, the bimolecular recombination constant of the kMC simulations at 300 K was extracted as k_2 =1.18×10^{-14} m^{3}s^{-1} (refer to Figure A.1 in the Appendix A). Which is roughly three orders of magnitude larger than k_2 = 1.7×10^{-17} m^{3}s^{-1}, which was measured by Toro *et al.* [14]. For 200 K, the extracted k_2 was 3.00×10^{-15} m^{3}s^{-1}, which is roughly one order of magnitude lower than the 300 K fit. A decrease in k_2 with temperature is predicted in the literature [37].

Utilising the integral of the Fermi–Dirac distribution over the DOS, the Pasveer model [32] for mobility in a Gaussian distribution, and the parameters in Table A.2 the DD curves, in Figure 4.4 were obtained.

Starting with the one at 300 K: In the forward bias regime, the DD curve decreases prematurely in comparison to the kMC curve, whereas in the reverse bias regime, the DD curve is consistently above the kMC. The difference between the blue DD curve and the simulated kMC curve is most-likely due to the underestimation of V_{OC} in DD simulations as explained by Upreti *et al.* [27]. If the curve is shifted by 0.13 V it alights better with the

kMC curve around V_{OC}. This offset is incorporated into Figure 4.7, in the dashed grey line. Clearly, the two simulated curves have similar shapes around V_{OC}. Following this grey dashed line: The vertical offset between the DD and kMC simulations (mostly in the reverse bias regime) can be attributed to the recombination type. As stated previously, in DD simulations recombination is bimolecular, whereas in kMC simulations there is geminate and non geminate recombination. From the plots in Figure 4.6, it is clear that: in the reverse bias regime recombination is mostly geminate, and around V_{OC} it is mostly non geminate. As such, right before V_{OC}, in the DD simulations, the recombination order corresponds more closely to that of the kMC, compared to the reverse bias regime.

For the 200 K curve: The DD simulations did not converge beyond -0.5 V, as per Figure 4.4(b), and the few simulated points do not follow the curve shape of the kMC simulations. This could be in part due to the very large k_2 value extracted from the kMC simulations and/or temperature dependent parameters that were not accounted for. On an important note, in this DD model, simulations with biases above V_{OC} generally do not converge, and as such are not displayed.

4.2.1 Temperature dependence

The previously measured EQEs, at SC and OC, for all three temperatures, were plotted in Figure 4.8(a). For both SC and OC EQEs, the curves at 300 K sit above the other two temperatures. Due to the temperature-dependent nature of charge carrier mobility, charges in a OSC lattice at 300 K have higher mobility than at 250 K and 200 K [24]. Thus, they are less likely to get trapped in the DOS, increasing the transport efficiency η_{CP}, which explains the consistently larger EQE (and IQE). Noticeably, the relative distance between the curves at SC is smaller than for OC. This could mean that thermal energy has a greater effect on the output current of the cell in OC conditions.

As for the low energy shoulder, previously mentioned in Section 4.1, the temperature of the OSC has a clear effect on the shoulder width (see Figure 4.8(b)). Just as in the work by Toro *et al.* [15], the width of the shoulder is reduced with temperature. Once again, bias plays no role. Notably, the shoulder, for this OSC, begins around 1.30 eV. Which is 0.10 eV above the non light biased EQE measurements. However, it is difficult to make a direct comparison between the light biased and dark measurements since these were not measured in the same PM6:Y6 cell. Additionally, in this Figure, the very low trap states are not visible, due to the increase in noise floor.

The previously calculated IQE spectra were normalised and plotted in Figure 4.9(a) for all three temperatures at SC and OC in three sets: the red set is composed of the OC curves, the blue set consists of the SC curves, and the mixed set comprises the SC and OC curves at 300 K. Through the red and blue curve set it is possible to discern a region in the IQE, between 1.36 eV 1.55 eV, that behaves differently than the low energy shoulder attributed to the S_0 to S_1 transition. This region is noticeably temperature dependent, the width reducing with increasing temperature, and bias independent, as per the total

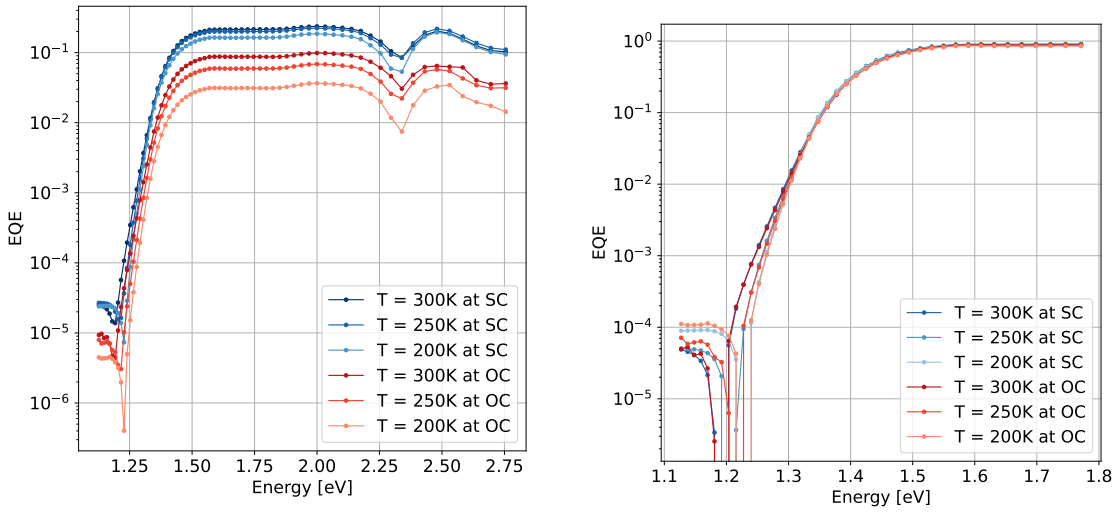

(a) (b)

Figure 4.8: **(a)** Experimentally obtained light biased SC EQE curves (in blue) and the light biased OC EQE curves (in red) for all three temperatures.; **(b)** Low energy range normalised at 1.55 eV light biased SC and OC EQE curves for all three temperatures.

overlap of the SC and OC (at 300 K) curves in this region.

Following a similar approach to Toro *et al.* [14], the activation energy for CT state dissociation was extracted from the curves in Figure 4.9(b), for four different points in the JV curve: at -2.00 V, SC, OC and 1.00 V. This was done by fitting the exponential curve:

$$\mathrm{EQE} = \mathrm{EQE}_0 \exp\left(-\frac{E_a}{k_B T}\right), \tag{4.1}$$

with EQE_0 as the EQE at infinite temperature, and E_a as the activation energy. In Table 4.2, are the extracted E_a for four different points in the EQE curve: 2.00 eV (donor peak) and for 1.55 eV (acceptor region), 1.40 eV (Temperature dependent region) and 1.26 eV (S_0 to S_1 transition). Noticeably, the difference in E_a between donor and acceptor regions is very small, which aligns with the lack of photon energy dependence noticed by Toro *et al.* [14]. Except for the -2.00 V point, the E_a at 1.40 eV peak behaved similarly to the donor and acceptor peaks. Which, could mean that this region is governed by CT dissociation, like the donor and acceptor regions. However, the vibronic transition peak E_a behaves completely differently than the other three points in the EQE spectrum. Which, aligns with the origin of the peak being different.

Additionally, there is a clear bias dependence. In the reverse bias regime, the E_a increases from -2.00 V to OC. Followed by a large decrease to negative values for -1.00 V. This bias dependency is due to the field dependence of η_{CC} and η_{CP} which directly affect the EQE, and naturally will affect the exponential fit. What is of interest in this Table, is consistent behaviour between the first three peaks for all biases, not necessarily the E_a values.

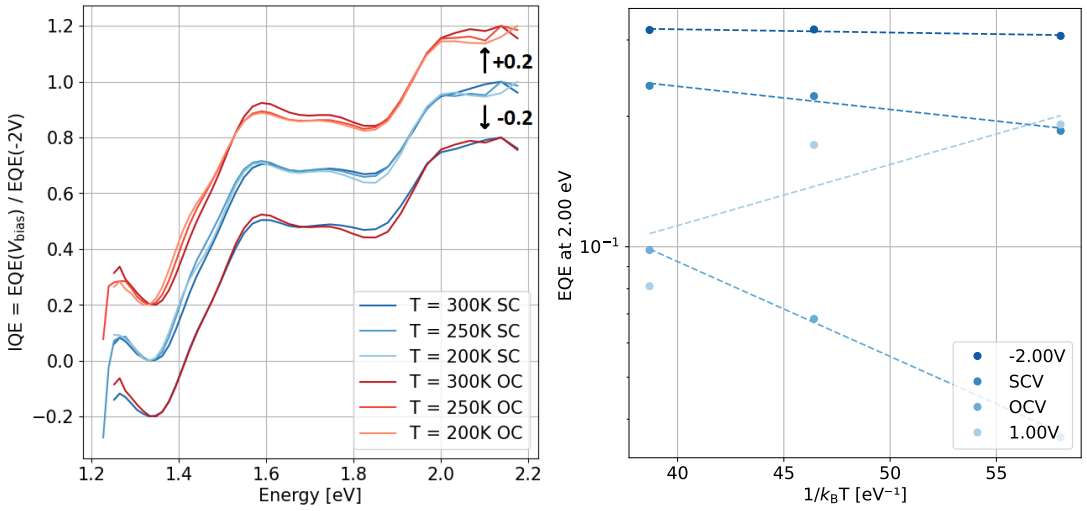

(a) (b)

Figure 4.9: **(a)**Normalised light biased IQE curves in three different sets: the blue set consists of the SC curves at 300 K, 250 K and 200 K, the red set (offset by 0.2 for easier analysis) composed of OC curves at the same three temperatures; the red and blue curve set (offset by -0.2) with the SC and OC curves at 300 K; **(b)** Exponential fit following Equation 4.1 at the donor peak at 2.00 eV, at -2.00 V, SC, OC and -1.00 V.

Table 4.2: E_a values at different biases and excitation energies

Bias [V]	E_a 2.00 eV [meV]	E_a 1.55 eV [meV]	E_a 1.40 eV [meV]	E_a 1.26 eV [meV]
-2.00	1.7 ± 0.9	1.8 ± 0.9	0 ± 1	42 ± 7
SC	12 ± 3	13 ± 3	13 ± 3	57 ± 5
OC	50 ± 2	52 ± 2	51 ± 2	104 ± 7
1.00	(-0.3 ± 0.2)×10^2	(-0.3 ± 0.2)×10^2	(-0.4 ± 0.2)×10^2	(0 ± 2)×10^1

4.2.2 Noise analysis

From Figure 4.2(a), it is evident that EQE reaches its noise floor at low incident photon energy (around 1.18 eV), which varies with applied bias, decreasing as the applied bias increases until V_{OC}, where the measurement has its lowest noise floor. In Figures A.7(a) and A.7(b), it becomes more evident that the noise floor increases again after V_{OC}. This bias dependency of the shot noise was also highlighted by Zeiske *et al.* [18], for their standard EQE measurements, reaching the minimum noise floor at 0.00 V. However, their measurements were not done under light biasing.

Another noise source to consider in light biased EQE measurements is the photon shot noise associated with the biasing light source, which will raise the noise floor as detailed by Zeiske *et al.* [18]. The effect of the photon shot noise along with the shot noise induced by the biasing light in the cell is clearly highlighted in the current versus energy plot in

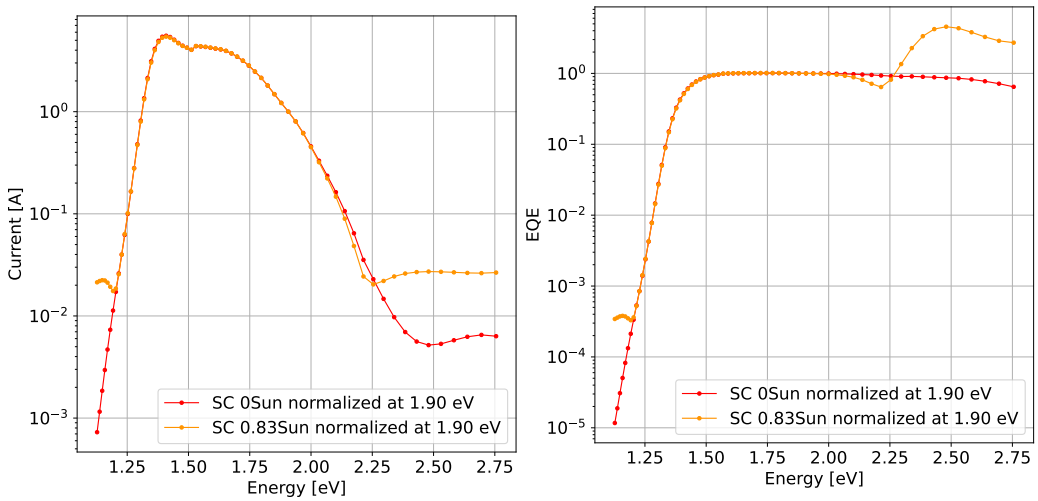

(a) (b)

Figure 4.10: Effect of the noise floor increase due to bias light in the **(a)** Cell current output against incident photon energy for light biased (in orange) and non light biased (in red) EQE measurements, at SC; **(b)** EQE measurements against incident photon energy for light biased (in orange) and non light biased (in red), at SC.

Figure 4.10(a). The only difference between the two curves is the addition of bias light. Beyond V_{OC}, the noise floor becomes increasingly irregular with bias and loses the curved shape. Which, could be attributed to an increase in the number of injected charges in the device.

Additionally, in these light biased plots, there is a bump in the high energy section (from 2.33 eV to 2.75 eV), which is inconsistent with the EQE curve shape in the literature for this material. Upon inspection of the current output of the cell during these measurements (see Figure A.9) it is clear that this bump is also a result of the increase of the noise floor due to the photon shot noise and illumination dependent cell shot noise. When divided by the high energy section of the Irradiance spectrum, as detailed by Equation 2.4, the noise floor will take on this bump like shape. This is made more evident when comparing the two plots in Figure 4.10.

4.2.3 Light biased vs non Light biased

Making a direct comparison between the light biased and non-light biased measurements is challenging because the two sets of measurements were conducted in different PM6:Y6 OSCs. Nevertheless, in Figure 4.11(a), the normalized IQE curves at 300 K are plotted for the light biased (solid line) and non-light biased (dotted line) cases. Generally, the light biased curves exhibit a less pronounced difference between the donor and acceptor regions. This suggests that the donor region may be more affected by excess recombination with non-modulated photo-generated charges in the light biased measurements.

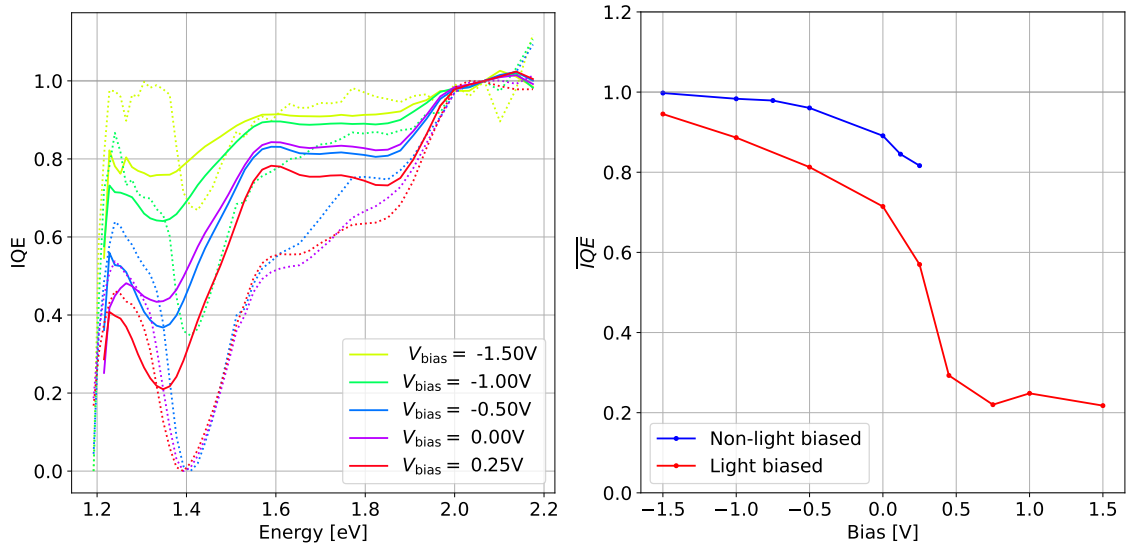

(a) (b)

Figure 4.11: **(a)** Normalised IQE curves for light biased (solid line) and non-light biased (dotted line) from -1.50 V to 0.25 V, at 300 K; **(b)** Experimentally obtained $\overline{\text{IQE}}(V)$ curves, for photon energies between 1.44 eV and 2.20 eV, at 300 K, for light biased (in red) and non light biased (in blue) measurements.

As for the $\overline{\text{IQE}}(V)$ (Figure 4.11(b)), calculated between 1.44 eV and 1.20 eV, the non-light biased curve (in blue) consistently remains above the light biased curve (in red), which could be attributed to increased recombination in the light biased curve. Nevertheless, both curves exhibit a similar non-linear decrease with electric bias.

4.2.4 Donor and Acceptor plateaus

The previously mentioned, the donor acceptor plateau difference is also bias dependent, as per Figure 4.11(a). Through Figure 4.2(b), it is also possible to see a difference in the IQE donor and acceptor regions (within the same curve). As the applied bias changes, the relative intensity of these two regions also changes. This same phenomenon was also noticed by *Zusan et al.* [23] for pBTTT:PCBM OSCs (from -2.00 V to 0.50 V or 0.25 V) with standard EQE measurements, which they attributed to the normalisation process. However, in a linear scale, the shape of the light biased EQE curves is also noticeably bias dependent (see Figure 4.12(a) for measurements at 250 K and Figure A.10 for 200 K and 300 K). As such, this shift is not due to the normalisation. This dependency was also observed by Brenner *et al.* [17] for PCPDTBT:PC70BM OSCs fabricated with the solvent additive octanedithiol and for TB7:PC70BM cells without the solvent. Which, they attributed to differences between excitons generated in the fullerene and polymer. Note that these OSC blends are FA based, which PM6:Y6 is not.

The relation between this plateau difference and the applied bias is concisely showcased

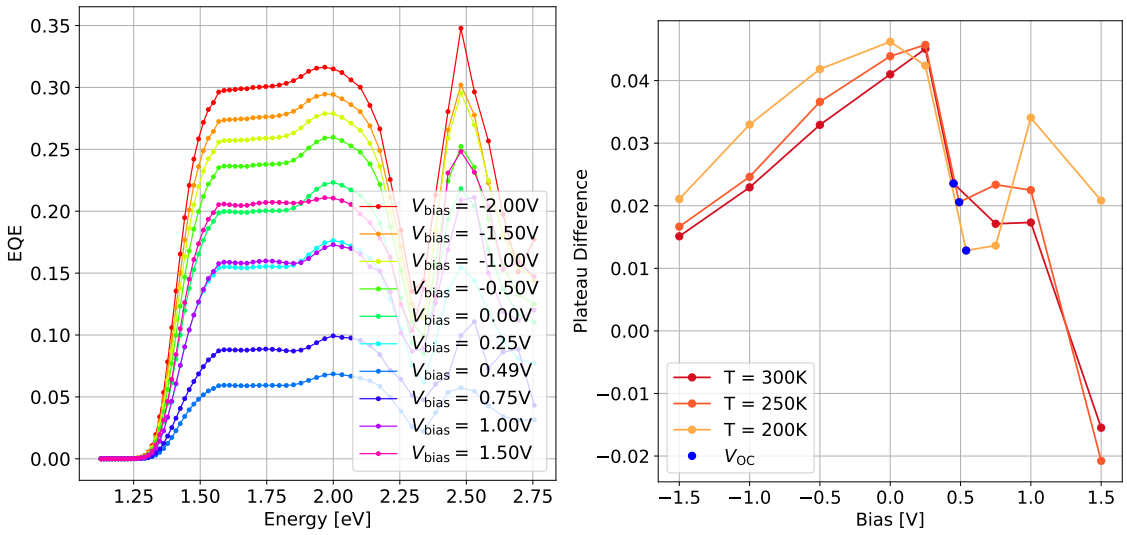

(a) (b)

Figure 4.12: **(a)** Experimentally obtained light biased EQE versus energy plots in a linear scale, of a PM6:Y6 solar cell at 250 K exposed to light bias and varying electrical bias from -2.00 V to 1.50 V; **(b)**Difference between the donor and the acceptor plateau averages plotted against applied bias. Averages taken from 1.95 eV to 2.30 eV and 1.55 eV to 1.90 eV for each material respectively.

in Figure 4.12(a), for all three temperatures. Since the entirety of the IQE spectrum decreases with decreasing internal field, it is not possible to determine if the donor or acceptor contribution to current is decreasing and or increasing relative to the other. What is clear from Figure 4.12(a) is that, before V_{OC}, as the internal field in the cell decreases, the plateau difference increases linearly, with a sudden decrease at V_{OC}. Beyond V_{OC}, the curves are less consistent. This could suggest that exciton dissociation is bias dependent, and phase (donor or acceptor) dependent.

4.2.5 Measurement Issues

During the EQE measurements, several issues manifested themselves:

- As previously mentioned, there might have been unintentional injected charge modulation and detection during the 200 K light biased EQE measurements.
- Encapsulation issues in the PM6:Y6 OSCs. Figure A.11, is a picture of the Deibel Lab PM6:Y6 used in the light biased EQE curves. Clearly, there seems to be some bleeding of the active material onto the electrodes, under the encapsulation glass. It is unclear what effects this has on the OCS, but it could be linked to decreased efficiency.
- The cells used in the light biased EQE plots were not state-of-the-art, showcasing a decreased V_{OC} and FF and PCE.

5

Conclusion

The focus of this thesis was to analyse the effect of electrical field and temperature on the quantum efficiencies of PM6:Y6 solar cells. With special focus on the $\overline{\text{IQE}}(V)$ curve.

Through this curve, it was possible to confirm the presence of significant photo-current in the forward bias regime and quantify an increase in recombination between injected and photo-generated charges. Notably, in these measurements, at OC conditions there is still photo-current exiting the cell. That is, at V_{OC} the photo-current must be offset by an injection current which in in line with the work by by Upreti *et al.*[27], guaranteeing net zero current at OC conditions.

The kMC simulation curve shape replicated the $\overline{\text{IQE}}(V)$ curve in the reverse and forward regime, revealing an electrical bias and temperature dependence in geminate recombination. This recombination type reached its maximum at the OC point. Moreover, it was possible to compare the kMC and experimental curves, in the reverse bias regime, with the DD model, at 300 K.

Furthermore, a brief analysis of the IQE spectrum shape at different biases points to bias and phase dependent exciton dissociation.

The lack of state-of-the-art PM6:Y6 OSCs, the injected charge modulation, and the possible issues caused by the cell encapsulation process make up the main challenges in this thesis. In this light, it would be important to replicate the $\overline{\text{IQE}}(V)$ curves with more efficiency and non encapsulated PM6:Y6 cells, as well as other OSC blends (e.g. P3HT:PCBM). This could be useful for a more detailed analysis around V_{OC}. Finally, conducting light and non-light biased EQE curve measurements on the same OSC would allow for direct comparison of the effects of light biasing on the EQE and IQE spectrum shape.

Bibliography

[1] J. M. Lourenço. *The NOVAthesis LaTeX Template User's Manual*. NOVA University Lisbon. 2021. URL: https://github.com/joaomlourenco/novathesis/raw/main/template.pdf (cit. on p. i).

[2] H. Choe et al. "Patent citation network analysis for the domain of organic photovoltaic cells: Country, institution, and technology field". In: *Renewable and Sustainable Energy Reviews* 26 (2013-10), pp. 492–505. ISSN: 13640321. DOI: 10.1016/j.rser.2013.05.037. URL: https://linkinghub.elsevier.com/retrieve/pii/S1364032113003407 (cit. on p. 1).

[3] Y. Wei et al. "Binary Organic Solar Cells Breaking 19% via Manipulating the Vertical Component Distribution". In: *Advanced Materials* 34 (33 2022-08). ISSN: 0935-9648. DOI: 10.1002/adma.202204718 (cit. on p. 1).

[4] W. Tress. "Device Physics of Organic Solar Cells: Drift-Diffusion Simulation in Comparison with Experimental Data of Solar Cells Based on Small Molecules". In: (2011), pp. 57–80 (cit. on pp. 3, 4, 6).

[5] "The Electronic Structure of Organic Semiconductors". In: *Electronic Processes in Organic Semiconductors*. John Wiley & Sons, Ltd, 2015. Chap. 1, pp. 1–86. ISBN: 9783527685172. DOI: https://doi.org/10.1002/9783527685172.ch1. eprint: https://onlinelibrary.wiley.com/doi/pdf/10.1002/9783527685172.ch1. URL: https://onlinelibrary.wiley.com/doi/abs/10.1002/9783527685172.ch1 (cit. on p. 2).

[6] C. Deibel and V. Dyakonov. "Polymer–fullerene bulk heterojunction solar cells". In: *Reports on Progress in Physics* 73 (9 2010-09), p. 096401. ISSN: 0034-4885. DOI: 10.1088/0034-4885/73/9/096401. URL: https://iopscience.iop.org/article/10.1088/0034-4885/73/9/096401 (cit. on pp. 3, 4).

[7] C. W. Tang. "Two-layer organic photovoltaic cell". In: *Applied Physics Letters* 48 (2 1986-01), pp. 183–185. ISSN: 0003-6951. DOI: 10.1063/1.96937. URL: http://aip.scitation.org/doi/10.1063/1.96937 (cit. on p. 3).

[8] J. Yuan et al. "Single-Junction Organic Solar Cell with over 15% Efficiency Using Fused-Ring Acceptor with Electron-Deficient Core". In: *Joule* 3 (4 2019-04), pp. 1140–1151. ISSN: 25424351. DOI: 10.1016/j.joule.2019.01.004. URL: https://linkinghub.elsevier.com/retrieve/pii/S2542435119300327 (cit. on pp. 4, 5, 8).

[9] K. Vandewal et al. "Efficient charge generation by relaxed charge-transfer states at organic interfaces". In: *Nature Materials* 13 (1 2014-01), pp. 63–68. ISSN: 1476-1122. DOI: 10.1038/nmat3807. URL: https://www.nature.com/articles/nmat3807 (cit. on p. 4).

[10] A. Köhler and H. Bässler. "The Electronic Structure of Organic Semiconductors". In: *Electronic Processes in Organic Semiconductors*. John Wiley & Sons, Ltd, 2015. Chap. 4, pp. 25–26. ISBN: 9783527685172. DOI: https://doi.org/10.1002/9783527685172.ch1. eprint: https://onlinelibrary.wiley.com/doi/pdf/10.1002/9783527685172.ch1. URL: https://onlinelibrary.wiley.com/doi/abs/10.1002/9783527685172.ch1 (cit. on p. 5).

[11] B. Sun et al. "Toward More Efficient Organic Solar Cells: A Detailed Study of Loss Pathway and Its Impact on Overall Device Performance in Low-Offset Organic Solar Cells". In: *Advanced Energy Materials* 13 (26 2023-07). ISSN: 1614-6832. DOI: 10.1002/aenm.202300980. URL: https://onlinelibrary.wiley.com/doi/10.1002/aenm.202300980 (cit. on p. 6).

[12] P. Peumans, A. Yakimov, and S. R. Forrest. "Small molecular weight organic thin-film photodetectors and solar cells". In: *Journal of Applied Physics* 93 (7 2003-04), pp. 3693–3723. ISSN: 0021-8979. DOI: 10.1063/1.1534621 (cit. on p. 6).

[13] S.-U.-Z. Khan et al. "Nonradiative Recombination via Charge-Transfer-Exciton to Polaron Energy Transfer Limits Photocurrent in Organic Solar Cells". In: *Advanced Energy Materials* 12 (19 2022-05). ISSN: 1614-6832. DOI: 10.1002/aenm.202200551. URL: https://onlinelibrary.wiley.com/doi/10.1002/aenm.202200551 (cit. on pp. 6, 8).

[14] L. Perdigón-Toro et al. "Barrierless Free Charge Generation in the High-Performance PM6:Y6 Bulk Heterojunction Non-Fullerene Solar Cell". In: *Advanced Materials* 32 (9 2020-03), p. 1906763. ISSN: 0935-9648. DOI: 10.1002/adma.201906763. URL: https://onlinelibrary.wiley.com/doi/10.1002/adma.201906763 (cit. on pp. 6, 9, 10, 16, 21, 28, 30).

[15] L. Perdigón-Toro et al. "Excitons Dominate the Emission from PM6:Y6 Solar Cells, but This Does Not Help the Open-Circuit Voltage of the Device". In: *ACS Energy Letters* 6 (2 2021-02), pp. 557–564. ISSN: 23808195. DOI: 10.1021/acsenergylett.0c02572 (cit. on pp. 6, 7, 21, 29).

[16] K. Vandewal et al. "Relating the open-circuit voltage to interface molecular properties of donor:acceptor bulk heterojunction solar cells". In: *Physical Review B - Condensed Matter and Materials Physics* 81 (12 2010-03). ISSN: 10980121. DOI: 10.1103/PhysRevB.81.125204 (cit. on pp. 7, 9, 21).

[17] T. J. K. Brenner, Z. Li, and C. R. McNeill. "Phase-Dependent Photocurrent Generation in Polymer/Fullerene Bulk Heterojunction Solar Cells". In: *The Journal of Physical Chemistry C* 115 (44 2011-11), pp. 22075–22083. ISSN: 1932-7447. DOI: 10.1021/jp208466t. URL: https://pubs.acs.org/doi/10.1021/jp208466t (cit. on pp. 7, 33).

[18] S. Zeiske et al. "Sensitivity of Sub-Bandgap External Quantum Efficiency Measurements of Solar Cells under Electrical and Light Bias". In: *ACS Photonics* 7 (1 2020-01), pp. 256–264. ISSN: 2330-4022. DOI: 10.1021/acsphotonics.9b01531. URL: https://pubs.acs.org/doi/10.1021/acsphotonics.9b01531 (cit. on pp. 8, 11, 19, 31).

[19] S. R. Cowan et al. "Intensity and wavelength dependence of bimolecular recombination in P3HT:PCBM solar cells: A white-light biased external quantum efficiency study". In: *Journal of Applied Physics* 113 (15 2013-04). ISSN: 0021-8979. DOI: 10.1063/1.4801920 (cit. on p. 8).

[20] T. J. K. Brenner et al. "White-light bias external quantim efficiency measurements of standard and inverted P3HT:PCBM photovoltaic cells". In: *Journal of Physics D: Applied Physics* 45 (41 2012-10), p. 415101. ISSN: 0022-3727. DOI: 10.1088/0022-3727/45/41/415101 (cit. on p. 8).

[21] N. A. Ran et al. "Charge Generation and Recombination in an Organic Solar Cell with Low Energetic Offsets". In: *Advanced Energy Materials* 8 (5 2018-02), p. 1701073. ISSN: 1614-6832. DOI: 10.1002/aenm.201701073. URL: https://onlinelibrary.wiley.com/doi/10.1002/aenm.201701073 (cit. on p. 8).

[22] Y. Liu et al. "Electric Field Facilitating Hole Transfer in Non-Fullerene Organic Solar Cells with a Negative HOMO Offset". In: *The Journal of Physical Chemistry C* 124 (28 2020-07), pp. 15132–15139. ISSN: 1932-7447. DOI: 10.1021/acs.jpcc.0c05654. URL: https://pubs.acs.org/doi/10.1021/acs.jpcc.0c05654 (cit. on p. 8).

[23] A. Zusan et al. "The Crucial Influence of Fullerene Phases on Photogeneration in Organic Bulk Heterojunction Solar Cells". In: *Advanced Energy Materials* 4 (17 2014-12), p. 1400922. ISSN: 16146832. DOI: 10.1002/aenm.201400922. URL: https://onlinelibrary.wiley.com/doi/10.1002/aenm.201400922 (cit. on pp. 8, 23, 33).

[24] H. Bassler. "Charge Transport in Disordered Organic Photoconductors a Monte Carlo Simulation Study". In: *physica status solidi (b)* 175 (1 1993-01), pp. 15–56. ISSN: 03701972. DOI: 10.1002/pssb.2221750102. URL: https://onlinelibrary.wiley.com/doi/10.1002/pssb.2221750102 (cit. on pp. 9, 26, 29).

[25] N. Felekidis, A. Melianas, and M. Kemerink. "The Role of Delocalization and Excess Energy in the Quantum Efficiency of Organic Solar Cells and the Validity of Optical Reciprocity Relations". In: *The Journal of Physical Chemistry Letters* 11 (9 2020-05), pp. 3563–3570. ISSN: 1948-7185. DOI: 10.1021/acs.jpclett.0c00945. URL: https://pubs.acs.org/doi/10.1021/acs.jpclett.0c00945 (cit. on pp. 9, 15).

[26] A. Armin et al. "Quantum Efficiency of Organic Solar Cells: Electro-Optical Cavity Considerations". In: *ACS Photonics* 1 (3 2014-03), pp. 173–181. ISSN: 2330-4022. DOI: 10.1021/ph400044k. URL: https://pubs.acs.org/doi/10.1021/ph400044k (cit. on p. 9).

[27] T. Upreti et al. "Slow Relaxation of Photogenerated Charge Carriers Boosts Open-Circuit Voltage of Organic Solar Cells". In: *The Journal of Physical Chemistry Letters* 12 (40 2021-10), pp. 9874–9881. ISSN: 1948-7185. DOI: 10.1021/acs.jpclett.1c02235. URL: https://pubs.acs.org/doi/10.1021/acs.jpclett.1c02235 (cit. on pp. 10, 14–17, 23–25, 28, 35, 41).

[28] A. Flamm. "Sensitive External Quantum Efficiency Measurements on Organic Solar Cells". In: (2023-05) (cit. on pp. 11, 13).

[29] S. Wilken et al. "Experimentally Calibrated Kinetic Monte Carlo Model Reproduces Organic Solar Cell Current–Voltage Curve". In: *Solar RRL* 4 (6 2020-06), p. 2000029. ISSN: 2367-198X. DOI: 10.1002/solr.202000029. URL: https://onlinelibrary.wiley.com/doi/10.1002/solr.202000029 (cit. on p. 14).

[30] T. Albes. "Kinetic Monte Carlo Simulations of Organic Solar Cells". In: (2018), pp. 33–37 (cit. on p. 14).

[31] M. Kemerink. *Documentation HolyHopper*. 2023-05 (cit. on p. 15).

[32] W. F. Pasveer et al. "Unified Description of Charge-Carrier Mobilities in Disordered Semiconducting Polymers". In: *Physical Review Letters* 94 (20 2005-05), p. 206601. ISSN: 0031-9007. DOI: 10.1103/PhysRevLett.94.206601. URL: https://link.aps.org/doi/10.1103/PhysRevLett.94.206601 (cit. on pp. 17, 28).

[33] Y. Roichman and N. Tessler. "Generalized Einstein relation for disordered semiconductors—implications for device performance". In: *Applied Physics Letters* 80 (11 2002-03), pp. 1948–1950. ISSN: 0003-6951. DOI: 10.1063/1.1461419 (cit. on p. 17).

[34] T. Kirchartz, J. Nelson, and U. Rau. "Reciprocity between Charge Injection and Extraction and Its Influence on the Interpretation of Electroluminescence Spectra in Organic Solar Cells". In: *Physical Review Applied* 5 (5 2016-05), p. 054003. ISSN: 2331-7019. DOI: 10.1103/PhysRevApplied.5.054003. URL: https://link.aps.org/doi/10.1103/PhysRevApplied.5.054003 (cit. on p. 17).

[35] S. Dhariwal, L. Kothari, and S. Jain. "Saturation of photovoltage and photocurrent in p-n junction solar cells". In: *IEEE Transactions on Electron Devices* 23 (5 1976-05), pp. 504–507. ISSN: 0018-9383. DOI: 10.1109/T-ED.1976.18436. URL: http://ieeexplore.ieee.org/document/1478450/ (cit. on p. 22).

[36] W. Tress et al. "Correlation of Absorption Profile and Fill Factor in Organic Solar Cells: The Role of Mobility Imbalance". In: *Advanced Energy Materials* 3 (5 2013-05), pp. 631–638. ISSN: 16146832. DOI: 10.1002/aenm.201200835. URL: https://onlinelibrary.wiley.com/doi/10.1002/aenm.201200835 (cit. on p. 23).

[37] G. Zuo et al. "General Rules for the Impact of Energetic Disorder and Mobility on Nongeminate Recombination in Phase-Separated Organic Solar Cells". In: *Physical Review Applied* 16 (3 2021-09), p. 034027. ISSN: 2331-7019. DOI: 10.1103/PhysRevApplied.16.034027. URL: https://link.aps.org/doi/10.1103/PhysRevApplied.16.034027 (cit. on p. 28).

A

Supplementary Tables and Figures

Table A.1: kinetic Monte Carlo parameters, taken from reference [27], for a simulated PM6:Y6 organic solar cells

Parameter	Value
Nearest neighbor distance, a_{NN} [nm]	1.8
LUMO acceptor, E_A LUMO [eV]	4.0
HOMO donor, E_D HOMO [eV]	5.44
Attempt-to-hop frequency electrons, $\nu_{0,e}$ [s^{-1}]	1×10^{11}
Attempt-to-hop frequency holes, $\nu_{0,h}$ [s^{-1}]	1×10^{11}
Energetic disorder electrons, σ_e [meV]	70
Energetic disorder holes, σ_h [meV]	70
Inverse exciton lifetime, ν_{ex} [s^{-1}]	1×10^{9}
Inverse CT state lifetime, ν_{CT} [s^{-1}]	3×10^{7}
Injection barrier height [eV]	0.2

Table A.2: Drift Diffusion parameters, taken from reference [27], for a simulated PM6:Y6 organic solar cells

Parameter	Value
Effective energy gap [eV]	1.4
Nearest neighbor distance, a_{NN} [nm]	1.8
Attempt-to-hop frequency electrons, $\nu_{0,e}$ [s^{-1}]	1×10^{11}
Attempt-to-hop frequency holes, $\nu_{0,h}$ [s^{-1}]	1×10^{10}
Energetic disorder [meV]	70
Injection barrier height [eV]	0.2

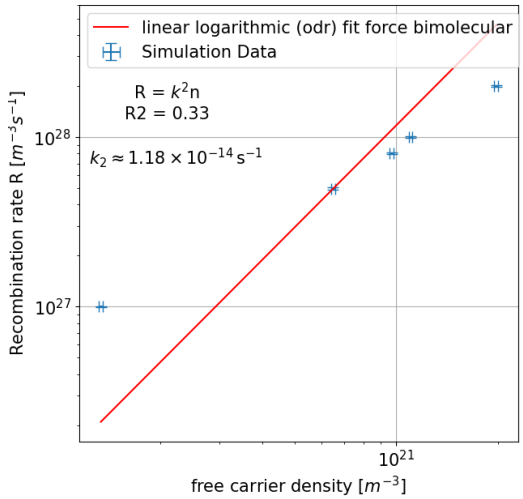

(a)

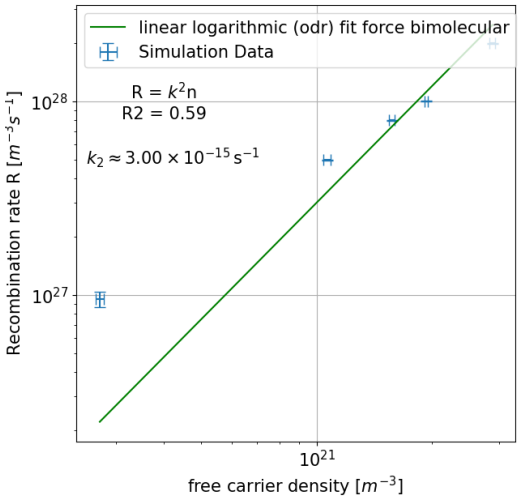

(b)

Figure A.1: Forced bimolecular fit obtained by fitting the recombination rate from current J_{rec} against the free charge carrier n obtained in the kMC simulations. The extracted k_2 is displayed in the plots, as well as the R2 of the fit **(a)** for 300 K **(b)** for 200 K

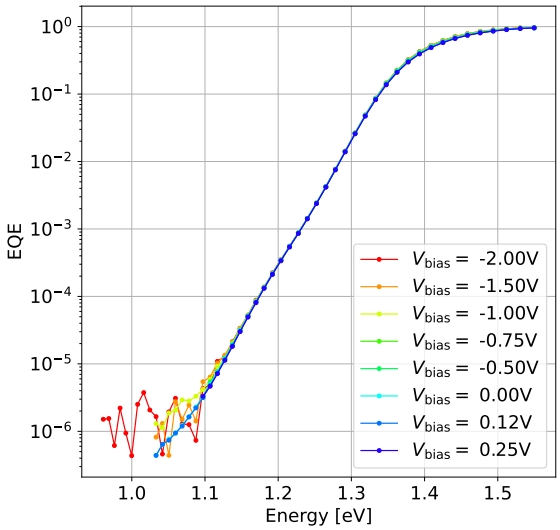

Figure A.2: Normalized at 1.72 eV, logarithmically scaled, low energy tail of the non light biased EQE curves with Varying electrical bias from -2,00 V to 0,25 V, obtained at 300 K ;

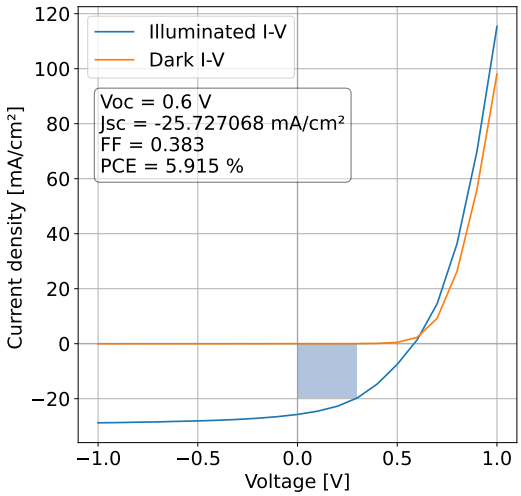

Figure A.3: JV curve of the measured PM6:Y6 OSC used in the light biased EQE plots. In blue, the illuminated curve and in orange the dark curve. In the illuminated curve the PCE is 5,915%, which is below what is expected for PM6:Y6 OSCs. The J_{SC} of ≈- 25,7 mA/cm^2 is typical for PM6:Y6, but the V_{OC} at 0,6 V is below typical Values. The FF is particularly low, reaching only 38.3%. The blue rectangle represents the FF.

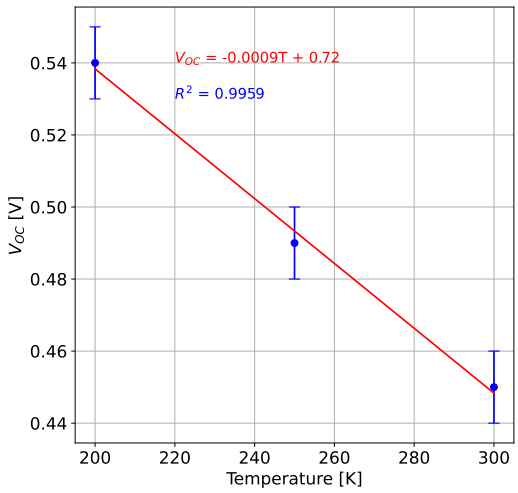

Figure A.4: V_{OC} versus temperature plot, detailing the linear relation between the measured V_{OC} at 300 K,250 K and 200 K.

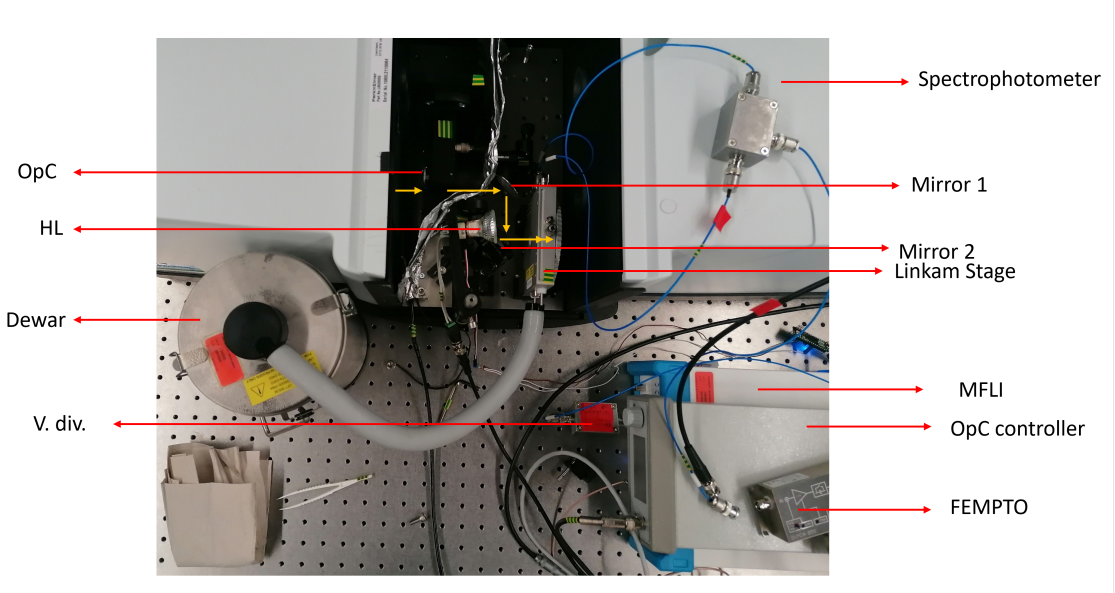

Figure A.5: Picture of experimental setup. With the light path in yellow.

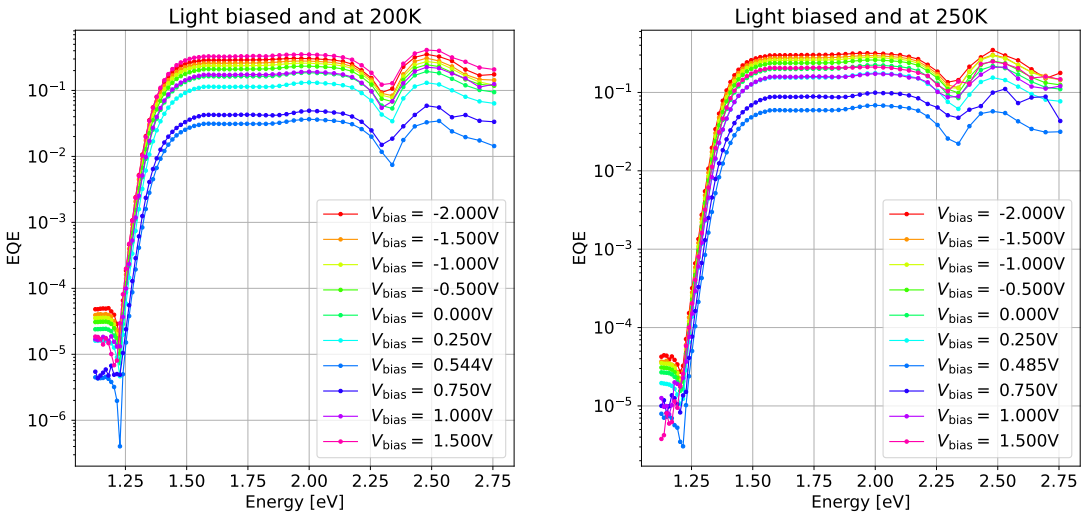

(a)

(b)

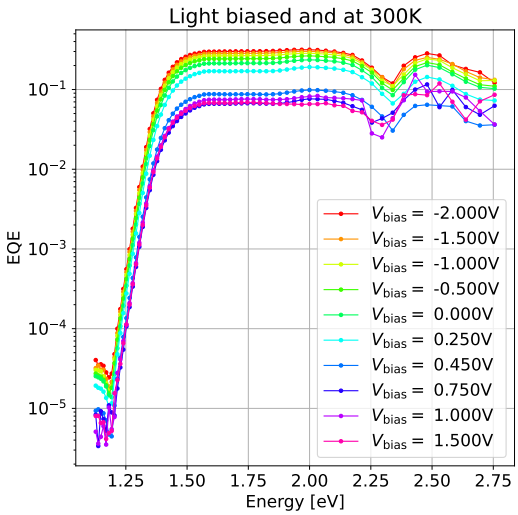

(c)

Figure A.6: EQE versus energy plots of the same PM6:Y6 solar cell at different temperatures (**(a)** 200 K,; **(b)** 250 K; **(c)** 300 K) exposed to bias light and varying electrical bias.

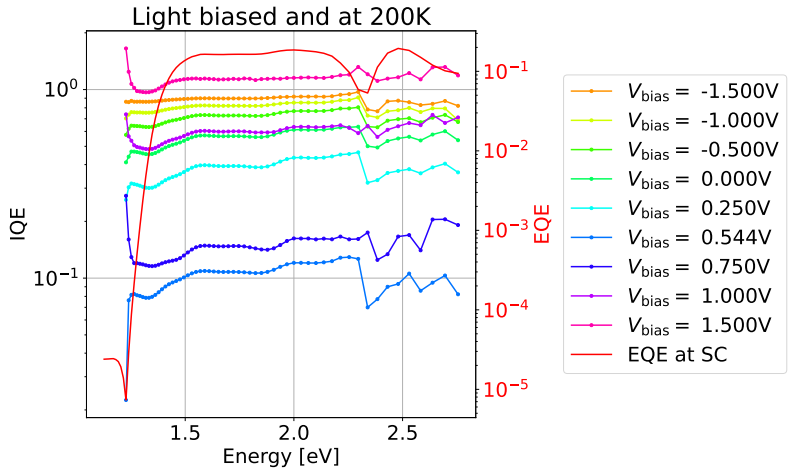

(a)

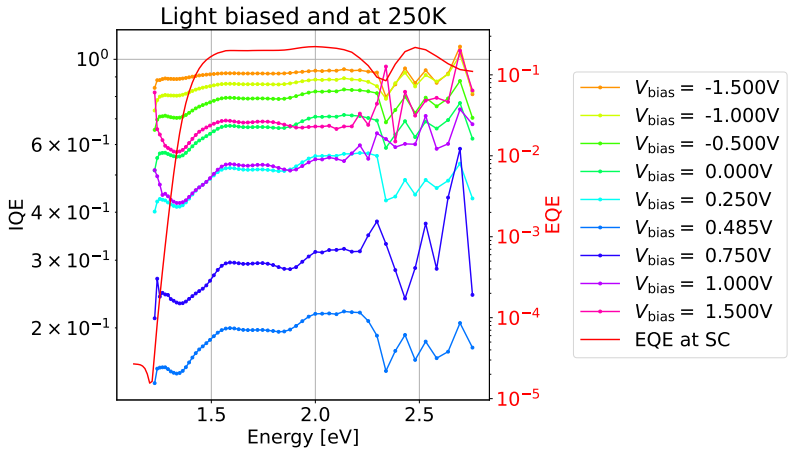

(b)

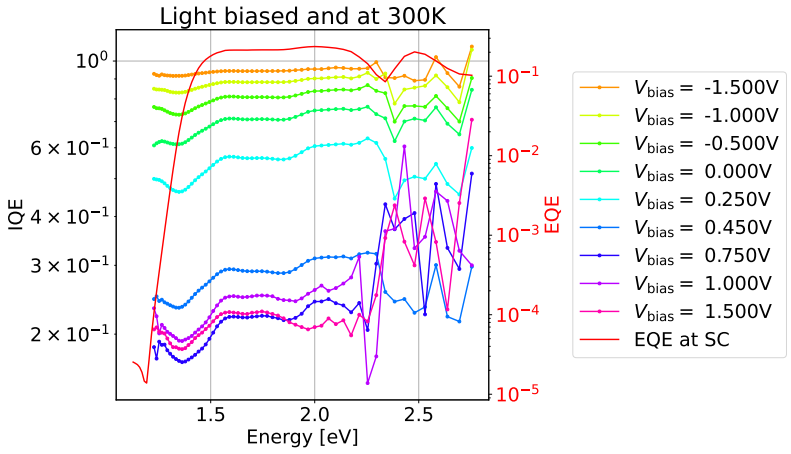

(c)

Figure A.7: IQE versus energy plots of the same PM6:Y6 solar cell exposed to bias light and varying electrical bias, at **(a)** at 200 K; **(b)** 250 K; and **(c)** 300 K.

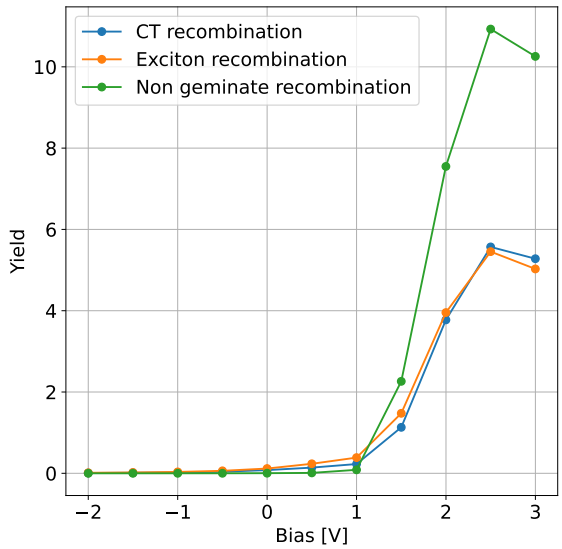

(a)

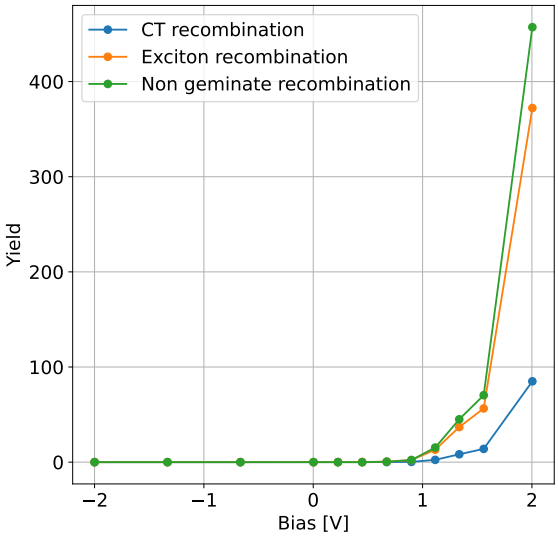

(b)

Figure A.8: Yield output of the kMC simulations versus bias. Non geminate recombination yield (in green), and exciton (in orange) and CT (in blue) recombination which refer to the recombination of excitons and CT states irrespective of their origin (photo-generated or not). **(a)** At 200 K; **(b)** and at 300 K. Note that at 200 K, at 2,00 V the non geminate recombination yield is ≈ 50 times smaller than at 300 K, due to decreased injection.

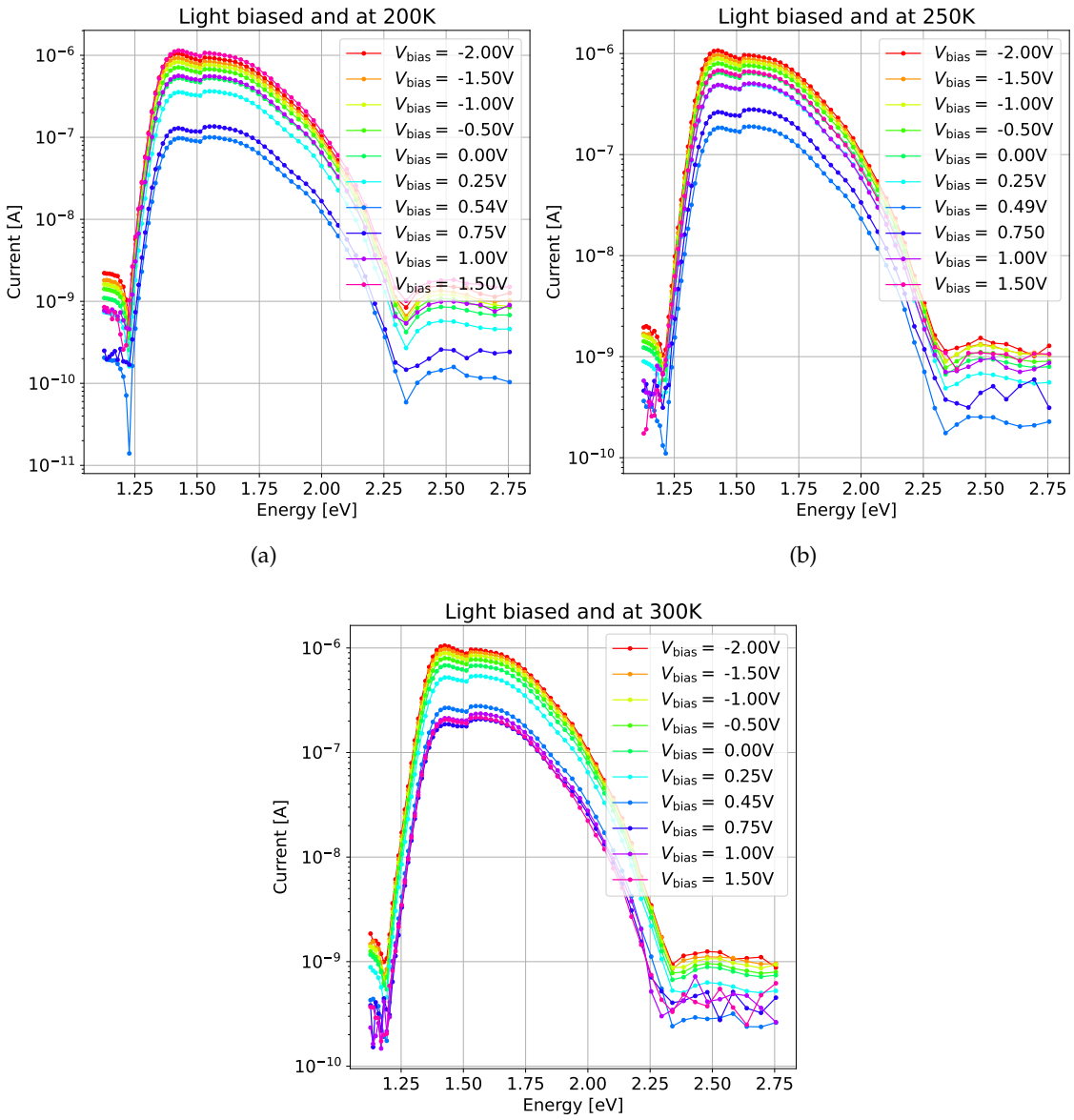

Figure A.9: Current output of the the same PM6:Y6 OSC during the EQE measurements at varying biases **(a)** at 200 K; **(b)** 250K; **(c)** and 300 K.

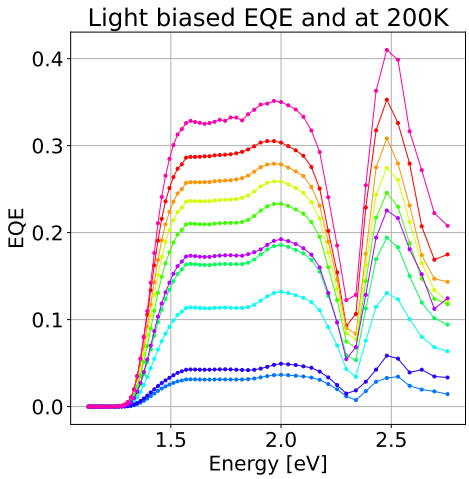

(a)

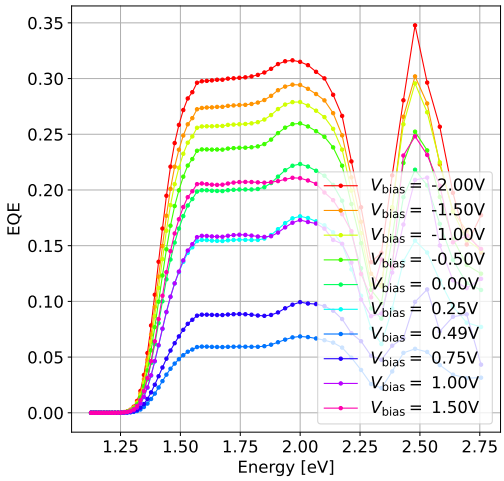

(b)

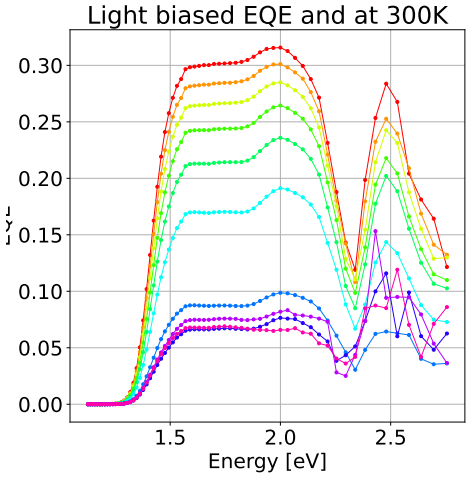

(c)

Figure A.10: Linear scale EQE versus energy plots of the same PM6:Y6 solar cell at different temperatures (200K **(a)**, 250K **(b)** and 300K **(c)**) exposed to bias light and varying electrical bias.

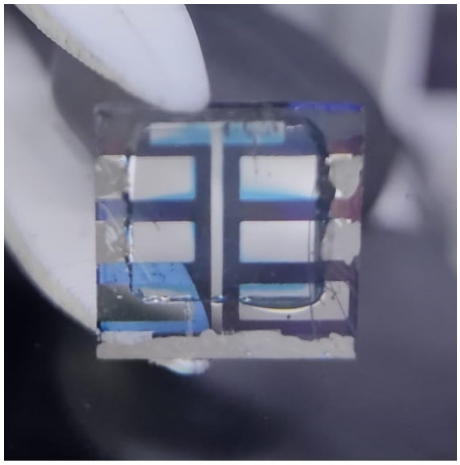

Figure A.11: Picture of the Deibel Lab PM6:Y6 used in the light biased EQE curves. There is some bleeding of the active material onto the contacts.

2023 Quantum efficiency of organic solar cells as a function of temperature and field: A study of PM6:Y6 Mónica Dyreby

NOVA
NOVA SCHOOL OF
SCIENCE & TECHNOLOGY